INTERNATIONAL ATOMIC ENERGY AGENCY
UNITED NATIONS EDUCATIONAL, SCIENTIFIC AND CULTURAL ORGANIZATION
INTERNATIONAL CENTRE FOR THEORETICAL PHYSICS

SMR/754 - 5

WORKSHOP ON
SCIENCE AND TECHNOLOGY OF THIN FILMS

(7 - 25 March 1994)

" Fundamentals of surface and thin films analysis "

presented by:

G. OTTAVIANI
Università degli Studi di Modena
Dipartimento di Fisica
Via Campi 213/A
41100 Modena
Italy

These are preliminary lecture notes, intended only for distribution to participants.

FUNDAMENTALS OF SURFACE AND THIN FILM ANALYSIS

Leonard C. Feldman
AT&T Bell Laboratories

James W. Mayer
Department of Materials Science and Engineering
Cornell University

North-Holland
New York • Amsterdam • London

CHAPTER

4

SPUTTER DEPTH PROFILES AND SECONDARY ION MASS SPECTROMETRY

4.1 Introduction

This chapter deals with the erosion of the sample by energetic particle bombardment. In this process, called sputtering, surface atoms are removed by collisions between the incoming particles and the atoms in the near surface layers of a solid. Sputtering provides the basis for composition depth profiling with surface analysis techniques either by analysis of the remaining surface with electron spectroscopies or analysis of the sputtered material. Here we describe the most widely used of these latter techniques, secondary-ion-mass spectroscopy (SIMS).

In previous chapters we have been concerned with the energies and yields of particles scattered from the target material under analysis. With Rutherford backscattering using MeV He ions, the energy loss along the inward and outward paths provides the depth information (Figure 4.1). In other analytical techniques the atoms to be identified must lie at the surface of the materials. For example, the observation depth in X-ray photo-electron and Auger-electron spectroscopy (XPS and AES) can be as small as 10–20 Å. In order to use XPS and AES to determine depth profiles, it is necessary to remove controlled thicknesses of the surface layer. This surface layer removal is carried out in materials analysis by bombarding the surface with low energy (0.5–20 keV) heavy ions, such as O^+ or Ar^+, which eject or sputter target atoms from the surface. The yield of sputtered

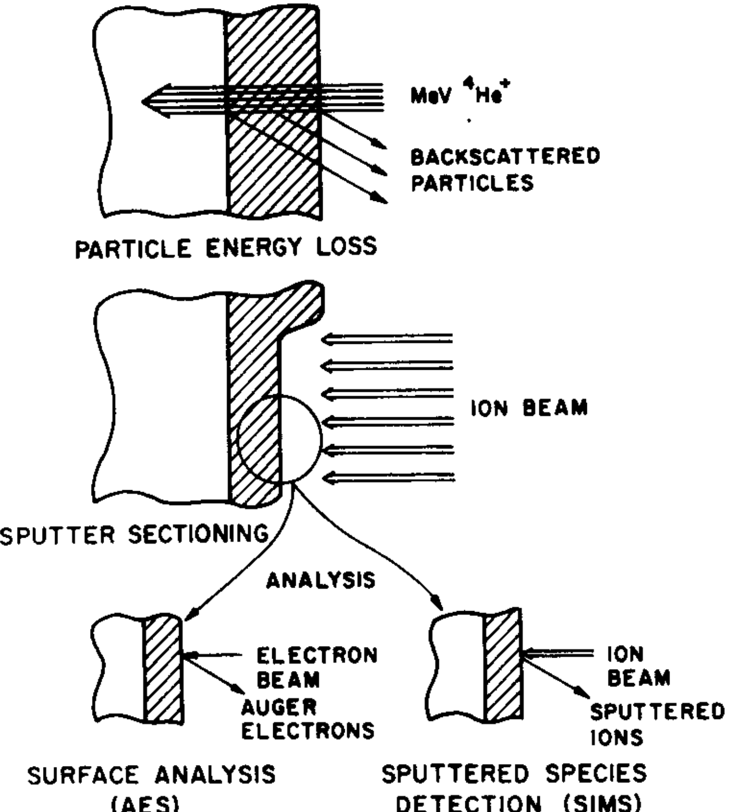

Figure 4.1 Schematic diagram of two approaches to obtain depth profiles in thin films. With particle energy loss techniques, the thickness of the layer is determined from the energy loss of the energetic particles. With sputter sectioning techniques the amount of material probed is determined by the sputtering yield. The surface composition can be directly analyzed either by electron spectroscopies or the amount of material removed by sputter species detection.

atoms, the number of sputtered atoms per incident ion, lies in the range of 0.5–20 depending upon ion species, ion energy, and target material. Surface sensitive techniques can then be used after each layer is removed to determine the composition of the new surface and hence deduce the depth profile of the atomic composition. It is also possible to analyze the sputtered atoms, generally the ionized species, to determine the composition of the sputter-removed materials. This technique of secondary-ion-mass spectroscopy or SIMS has been used extensively in depth profiling. One can also measure the characteristic radiation emitted from excited sputtered ions or atoms to determine the composition of the sputter removed material.

For sputtering, it is the energy lost in elastic collisions with the atomic cores—termed *nuclear energy loss*—that determines the energy transfer to and eventual ejection of surface atoms. For backscattering or nuclear analysis, the energetic particles lose energy primarily through electron excitation and ionization in inelastic collisions with atomic electrons—termed *electronic energy loss*. A good assumption is that electronic energy loss and nuclear energy loss can be treated separately and independently. In Chapter 3 we described electronic energy loss and showed that the amount of nuclear energy loss was small. In the sputtering regime the nuclear energy loss dominates.

4.2 Sputtering by Ion Bombardment—General Concepts

Surfaces of solids erode under ion bombardment. The erosion rates are characterized primarily by the sputtering yield Y, which is defined as

$$Y = \text{Sputtering yield} = \frac{\text{Mean number of emitted atoms}}{\text{Incident particle}}. \quad (4.1)$$

The sputtering yield depends on the structure and composition of the target material, the parameters of the incident ion beam, and the experimental geometry. Measured values of Y cover a range of over seven decades; however, for the medium mass ion species and keV energies of general interest in depth profiles, the values of Y lie between 0.5 and 20. The sputtering yields of MeV light ions for most materials are of the order of 10^{-3}. Consequently, Rutherford backscattering analysis will cause the sputtering of only a small fraction of a monolayer during a typical analysis (see Section 3.11).

Sputtering yields can be accurately predicted by theory for single element materials. Figure 4.2 shows the energy and incident particle dependence of the sputtering yield of Si. The experimental values, in good agreement with calculations (solid line) by Sigmund (1981), are based on nuclear energy loss mechanisms and the sharing of this energy loss among the large number of atoms which define the collision cascade. For any given ion–target combination it is desirable to refer to tabulated values or to determine the yield experimentally.

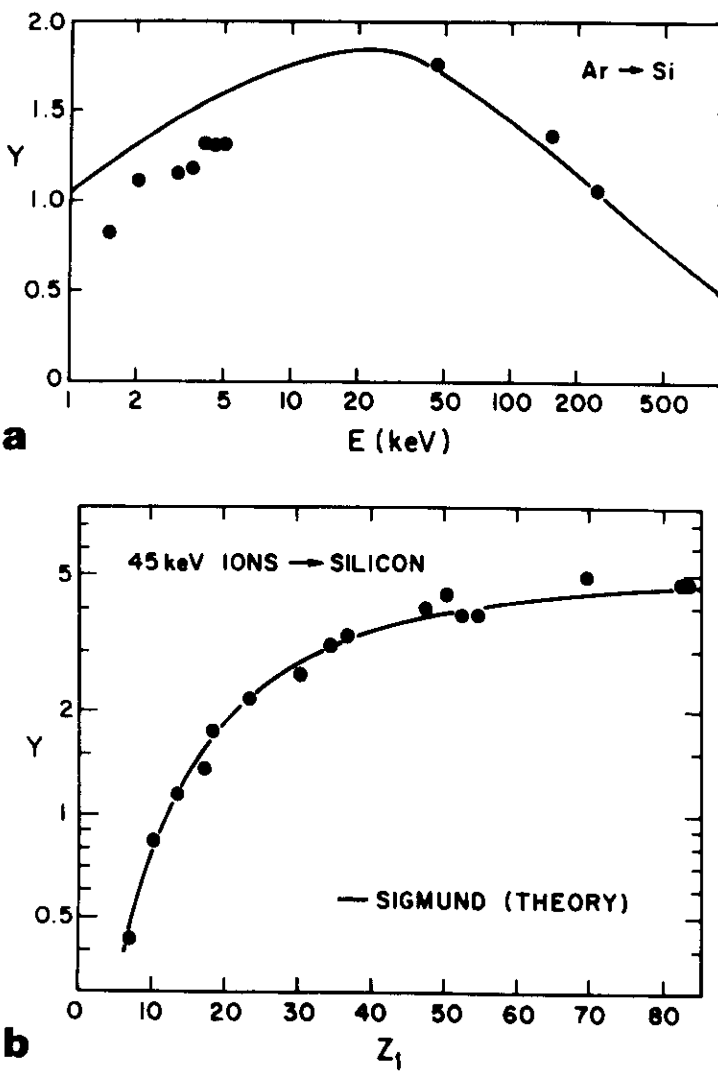

Figure 4.2 (a) Energy dependence of the Ar sputtering yield of Si and (b) incident ion dependence of the Si sputtering yield. The solid line represents the calculations of Sigmund and the data is from Andersen and Bay (1981).

There are a number of review articles and books on the topic of sputtering that are listed in the references at the end of this chapter.

In the sputtering process, atoms are ejected from the outer surface layers. The bombarding ion transfers energy in collisions to tar-

coils (Figure 4.3). Some of these backward recoils (about 1–2 atoms for a 20 keV Ar ion incident on Si) will approach the surface with enough energy to escape from the solid. It is these secondary recoils which make up most of the sputtering yield. For example, for the case of Ar on Si, target recoils in the backward direction toward the surface are kinematically forbidden as is Ar backscattering (see Chapter 2). The sputtering process involves a complex series of collisions (the collision cascade) involving a series of angular deflections and energy transfers between many atoms in the solid. It is possible to simulate the sputtering process on a computer via a series of binary events, but such simulations do not readily yield the dependencies of the sputtering process on various experimental parameters. The problem has been approached based on transport theory, which considers the dynamics of the collision cascade and derives the total energy flux in the backward direction. Such a derivation is beyond the scope of this book. However, we do extract the important parameters based on nuclear energy loss concepts. Clearly the most important parameter in the process is the energy deposited at the surface.

The sputtering yield should be proportional to the number of displaced or recoil atoms. In the linear cascade regime that is applicable for medium mass ions (such as Ar), the number of recoils is proportional to the energy deposited per unit depth in nuclear energy loss. We can then express the sputtering yield Y for particles incident normal to the surface as

$$Y = \Lambda F_D(E_0), \tag{4.2}$$

where Λ contains all the material properties such as surface binding energies and $F_D(E_0)$ is the density of deposited energy at the surface

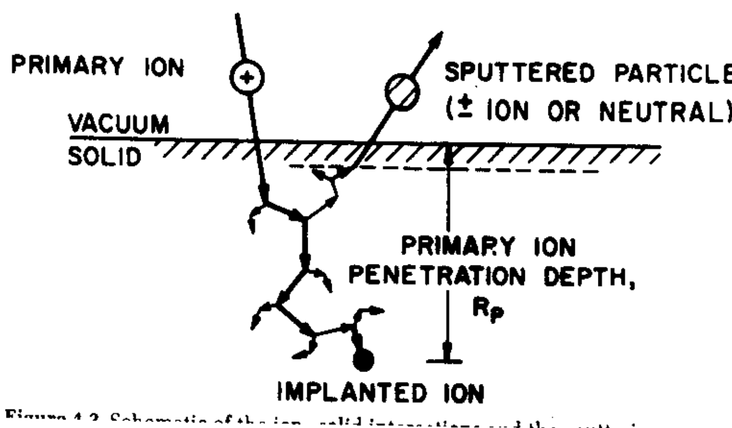

and depends on the type, energy, and direction of the incident ion and the target parameters Z_2, M_2, and N.

The deposited energy at the surface can be expressed as

$$F_D(E_0) = \alpha N S_n(E_0), \tag{4.3}$$

where N is the atomic density of target atoms, $S_n(E)$ is the nuclear stopping cross section, and $NS_n(E) = dE/dx|_n$ the nuclear energy loss. In this equation α is a correction factor which takes into account the angle of incidence of the beam to the surface and contributions due to large angle scattering events which are not included in the development. The sputtering yield is calculated in Section 4.4.

The evaluation of $S_n(E)$ rests on the collision cross section for energy transfer to a substrate atom. In the keV sputtering regime where the particle velocity is much less than the Bohr velocity, screening of the nuclear charge by the electrons must be included in the description of the collisions. The procedure to obtain the sputtering yield is to first treat a screened potential from a description of the Thomas–Fermi approximations (Section 4.9), and then derive the collision cross section based on a screened potential to obtain the nuclear stopping cross section (Section 4.3).

4.3 Nuclear Energy Loss

A charged particle penetrating a solid loses energy through two processes: (1) energy transfer to electrons, electronic energy loss; and (2) energy transfer to the atoms of the solid, nuclear energy loss. In both cases the interaction is basically of a Coulomb type; for the electronic case it is pure Coulomb (see Chapter 3) while in the nuclear case it is a form of screened Coulomb potential. The two mechanisms have different energy dependencies—in the electronic case there is a peak in the cross section at projectile energies of the order of 0.1–1.0 MeV for light projectiles; in the nuclear case the peak in the loss cross section is at much lower energy, of the order of 0.1–10 keV. In penetration theory the electronic and nuclear energy losses are treated as uncorrelated and simply summed. In many cases, one or the other contribution is negligible and is simply ignored. Sputtering is governed by the energy deposited via nuclear energy loss at the surface of a solid. This is the mechanism which transfers momentum and energy to the atoms of the solid resulting in energetic secondaries and sputtering. In this section we give a simple description of nuclear energy loss and compare it to the more sophisticated treatments. As in other sections

of this text our aim is to provide a simple mathematical description of the process in order to provide some insight into the quantitative understanding of the physics.

The derivation of nuclear energy loss uses two main assumptions: (1) a simple screened Coulomb potential and (2) the impulse approximation.

The interaction potential between two atoms Z_1 and Z_2 can be written in the form of a screened Coulomb potential (Section 4.9) using χ as the screening function,

$$V(r) = \frac{Z_1 Z_2 e^2}{r} \cdot \chi\left(\frac{r}{a}\right), \tag{4.4}$$

where a is the Thomas–Fermi screening radius for the collision

$$a = \frac{0.885 a_0}{(Z_1^{1/2} + Z_2^{1/2})^{2/3}}. \tag{4.5}$$

The values of a lie between 0.1 and 0.2 Å for most interactions. We take as a screening function

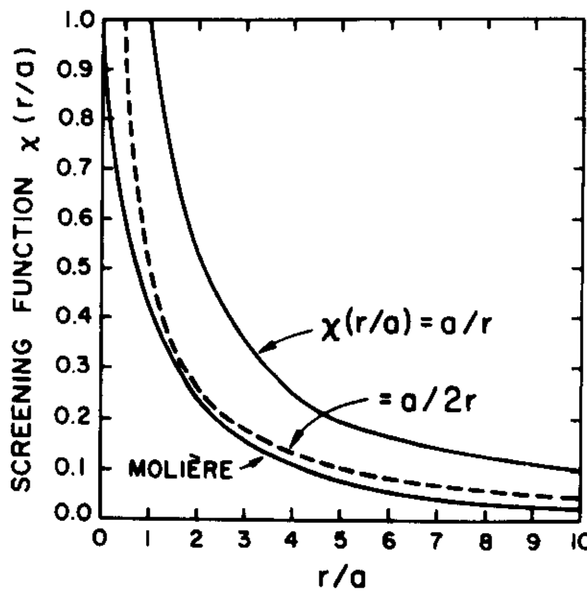

Figure 4.4 The screening function χ in the Molière approximation. At $r = a$, the value of the screening function has dropped to about 0.4 in support of the choice of a as an approximation for the atomic size. Shown also are the screening functions $\chi = a/r$ and $a/2r$.

$$\chi(r/a) = a/2r \tag{4.6}$$

leading to a potential of the form

$$V(r) = \frac{Z_1 Z_2 e^2 a}{2r^2}. \tag{4.7}$$

The screening functions a/r and $a/2r$ are illustrated in Figure 4.4 and the latter reasonably follows the shape of the more accurate Molière potential for $r/a > 1$. The $1/r^2$ potential is not a good approximation for $r/a < 1$ since it does not go into the pure Coulomb form as $r \to 0$. For low energy particles as used in sputtering, this is not a severe problem since the distance of closest approach is large thus preventing interactions at small r.

The impulse approximation is appropriate for the small-angle large-impact parameter collisions that dominate the sequence of scatterings which determine the charged particle trajectory. We have used this approximation in the derivation of electronic stopping given in Chapter 3. In the impulse approximation the change in momentum is given by

$$\Delta p = \int_{-\infty}^{\infty} F_\perp \, dt \tag{4.8}$$

or

$$\Delta p = \frac{1}{v} \int_{-\infty}^{\infty} F_\perp \, dx, \tag{4.9}$$

where $F_\perp$ is the component of the force acting on the ion perpendicular to its incident direction. By using the geometry of Figure 3.3, the force may be written with $r = \sqrt{x^2 + b^2}$ as

$$F_\perp = -\frac{\partial V(r)}{\partial y} = -\frac{\partial V(\sqrt{x^2 + b^2})}{\partial b}. \tag{4.10}$$

Then

$$\Delta p = -\frac{1}{v} \frac{\partial}{\partial b} \int_{-\infty}^{\infty} V(\sqrt{x^2 + b^2}) \, dx \tag{4.11}$$

or, using Eq. (4.7),

$$\Delta p = -\frac{1}{v} \frac{\partial}{\partial b} \int_{0}^{\infty} \frac{Z_1 Z_2 e^2 a}{(x^2 + b^2)} \, dx, \tag{4.12}$$

which reduces to

$$\Delta p = \frac{\pi Z_1 Z_2 e^2 a}{2vb^2}. \tag{4.13}$$

The energy transferred, T, to the recoiling nucleus is

$$T = \frac{\Delta p^2}{2M_2}, \qquad T = \frac{\pi^2 Z_1^2 Z_2^2 e^4 a^2}{8M_2 v^2 b^4}. \tag{4.14}$$

The cross section $d\sigma(T)$ for transfer of energy between T and $T + dT$ is

$$d\sigma = -2\pi b \, db$$

or

$$d\sigma = -\frac{\pi^2 Z_1 Z_2 e^2 a}{8\sqrt{(M_2/M_1)E}} T^{-3/2} \, dT, \tag{4.15}$$

where $E = M_1 v^2/2$.

It is convenient to express this result in terms of the maximum energy transfer T_m, where

$$T_m = \frac{4M_1 M_2}{(M_1 + M_2)^2} E,$$

then

$$d\sigma = -\frac{\pi^2 Z_1 Z_2 e^2 a}{4 T_m^{1/2}} \frac{M_1}{(M_1 + M_2)} T^{-3/2} \, dT. \tag{4.16}$$

The nuclear stopping cross section S_n is given by

$$S_n = -\int T \, d\sigma$$

or

$$S_n = \frac{\pi^2 Z_1 Z_2 e^2 a}{2T_m^{1/2}} \left(\frac{M_1}{M_1 + M_2} \right) T^{1/2} \Big|_0^{T_m}$$

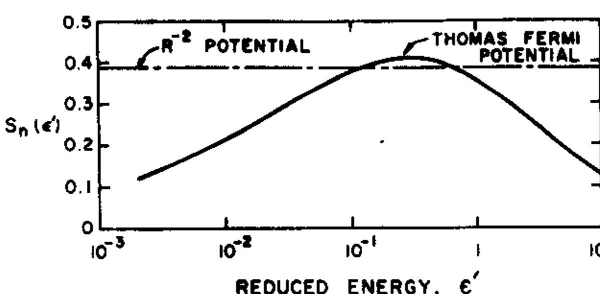

Figure 4.5 Reduced nuclear stopping cross section $S_n(\epsilon')$ (or $d\epsilon'/d\rho$) as a function of ϵ'. The Thomas-Fermi curve represents the most accurate value of S_n for the Thomas-Fermi potential; the horizontal line is the result for an R^{-2} potential [Eq. (4.17)].

$$S_n = \frac{\pi^2 Z_1 Z_2 e^2 a M_1}{2\,(M_1 + M_2)}. \tag{4.17}$$

The nuclear energy loss is given by

$$\left.\frac{dE}{dx}\right|_n = NS_n, \tag{4.18}$$

where N is the number of atoms/volume in the solid. Note that in this approximation $dE/dx|_n$ is independent of energy, i.e.,

$$\left.\frac{dE}{dx}\right|_n = N\frac{\pi^2}{2} Z_1 Z_2 e^2 a \frac{M_1}{M_1 + M_2}. \tag{4.19}$$

Figure 4.5 compares this energy independent value to the values of the nuclear energy loss using the Thomas-Fermi potential.

Figure 4.5 follows the description of Lindhard in which the nuclear energy loss is expressed in terms of a reduced energy ϵ' given by the ratio of the Thomas screening distance to the distance of closest approach,

$$\epsilon' = \frac{M_2}{M_1 + M_2} E \cdot \frac{a}{Z_1 Z_2 e^2} \tag{4.20a}$$

and a reduced length ρ based on a cross section πa^2 and an energy ratio T_m/E,

$$\rho = xNM_2 4\pi a^2 M_1/(M_1 + M_2)^2. \tag{4.20b}$$

This form is then generally useful in that the stopping power for any combination of projectile and target at any energy can be found. In this formalism, $d\epsilon'/d\rho = S_n(\epsilon')$ so that using Eqs. (4.20a) and (4.20b)

$$\left.\frac{dE}{dx}\right|_n = 4\pi a N Z_1 Z_2 e^2 \frac{M_1}{M_1 + M_2} S_n(\epsilon'), \tag{4.21}$$

where $S_n(\epsilon')$ depends on the form of $V(r)$. In terms of the value of $(dE/dx)_n$ derived in Eq. (4.19), the energy-independent value of the nuclear energy loss in reduced units of energy and length is 0.393. This is slightly different than the value given by Lindhard et al. (1963) since we have used an impulse approximation while these authors evaluate the scattering integral more completely.

Note that our approximation, Eq. (4.19), gives the correct order of magnitude for the stopping power but deviates considerably in the energy dependence. Most significantly, it does not display the $1/E$ dependence at high energy. This is a result of using a $1/r^2$ potential rather than a $1/r$ potential. Clearly, the $1/r^2$ approximation is worst at high energies where close collisions are important. Accurate values of the nuclear energy loss $(dE/dx)_n$ can be derived from Eq. (4.21) and Figure 4.5, which gives $S_n(\epsilon')$ for the more accurate Thomas-Fermi potential (Section 4.9).

For 1 keV Ar ions incident on a medium mass target, Cu, $a =$ 0.103 Å and $\epsilon' = 0.008$, and, for 10 keV O ions on Cu, $a = 0.115$ and $\epsilon' = 0.27$. (Ar and oxygen are generally used in sputter profiling.) Thus for ion energies from 1 to 10 keV, the values of ϵ' are in the range of 0.01-0.3; this is a range just below the plateau of dE/dx. As an approximation to estimate the magnitude of $dE/dx|_n$, an energy independent value (a rough average) of $S_n(\epsilon') \cong 0.39$ can be used. For Ar in Cu, $dE/dx|_n \cong 124$ eV/Å, and, for oxygen in Cu, $dE/dx|_n \cong 32$ eV/Å.

4.4 Sputtering Yield

The yield Y of sputtered particles from single element amorphous targets was expressed in Eq. (4.2) as the product of two terms: one, Λ, containing material parameters and the other, F_D, the deposited energy. The derivation of Λ involves a description of the number of recoil atoms that can overcome the surface barrier and escape from the solid. The details of the derivation for the linear cascade regime are given by Sigmund. The result is

$$\Lambda \cong \frac{0.042}{NU_0}\ (\text{Å/eV}), \tag{4.22}$$

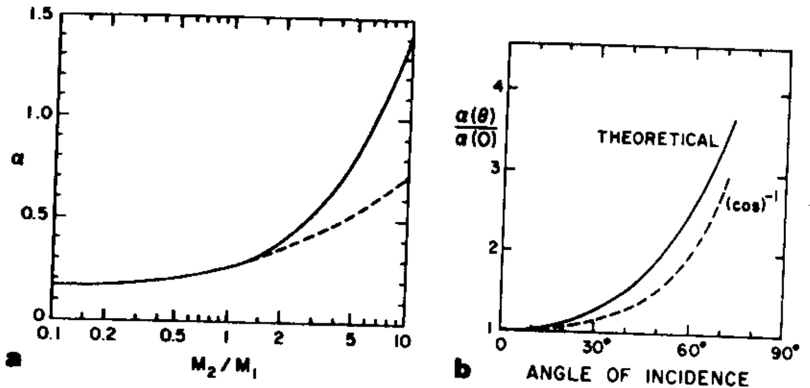

Figure 4.6 Factor α occurring in the backward-sputtering yield formula (4.3). (a) Dependence on mass ratio M_2/M_1: (——) theoretical, evaluated for elastic scattering only, no surface correction applied; (- - -) interpolated from experimental sputtering yields for 45 keV ions on Si, Cu, Ag, and Au. (The difference is mainly due to the neglect of the surface correction at large mass ratios.) (b) Dependence on angle of incidence: (——) theoretical for Ar ions on Cu; (- - -) $(\cos\theta)^{-1}$ dependence, valid mainly in the high-velocity limit. [From Sigmund, 1981.]

where N is the atomic density (in Å^{-3}) and U_0 (in eV), the surface binding energy. The value of U_0 can be estimated from the heat of sublimation (≅heat of vaporization) and typically has values between 2 and 4 eV. For the deposited energy, Eq.(4.3),

$$F_D = \alpha \cdot N \cdot S_n,$$

the value of α is a function of the mass ratio and ranges between 0.2 and 0.4 as shown in Figure 4.6. The value of α increases with the angle of incidence because of increased energy deposition near the surface. A reasonable average value for normal incidence sputtering with medium mass ions is $\alpha = 0.25$.

For Ar incident on Cu, the value of $NS_n = 124$ eV/Å. The surface binding energy, U_0 is ∼3 eV based on a heat of vaporization of ≃3 eV. The sputtering yield with $N = 8.5 \times 10^{-2}$ atoms/Å^3 is

$$Y = \frac{0.042 \times 0.25 \times 124 \text{ eV/Å}}{8.45 \times 10^{-2}/\text{Å}^3 \times 3 \text{ eV}} = 5.1,$$

which is in reasonable agreement with measured values of about 6.

These estimates hold for the ideal case of an amorphous single-element target. The sputtering yields from single crystal, polycrystalline, or alloy targets may deviate significantly from the simple estimates above. With polyatomic targets preferential sputtering of one of

the elements can lead to changes in composition of the surface layer. These changes will be reflected in the Auger yields which give the composition of the altered, not original, layer. Another complication is ion beam mixing (redistribution within the collision cascade), which can lead to broadening of the interface when profiling layered targets. In many of these cases it is possible to use Rutherford backscattering to establish layer thicknesses and the concentration of the major constituents. This will then provide a calibration for the sputter profile.

4.5 Secondary Ion Mass Spectrometry (SIMS)

Surface layers are eroded by the sputtering process and hence the relative abundance of the sputtered species provide a direct measure of the composition of the layer that has been removed. Sputtered

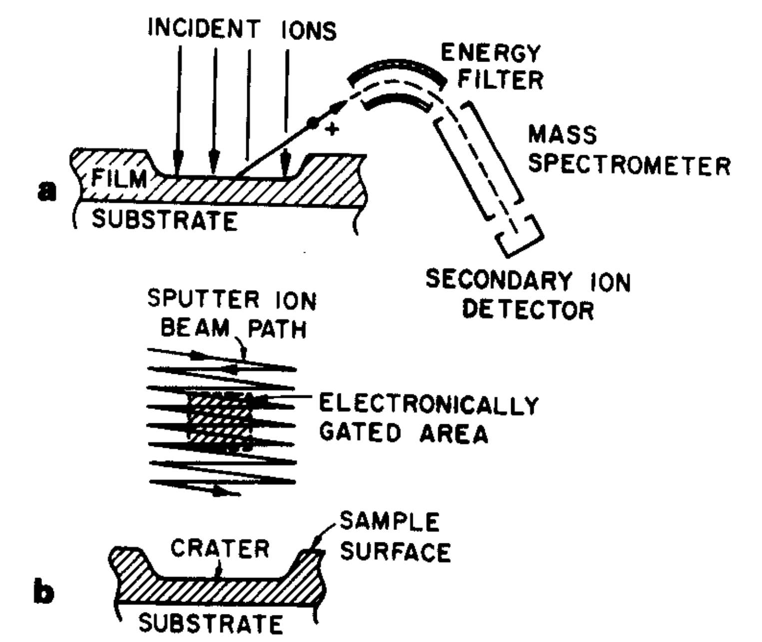

Figure 4.7 (a) Schematic of the SIMS apparatus. An incident ion beam results in sputtered ionic species which are passed through an electrostatic energy filter and a mass spectrometer and finally detected by an ion detector. (b) The beam is usually swept across a large area of the sample and the signal detected from the central portion of the sweep. This avoids crater edge effects.

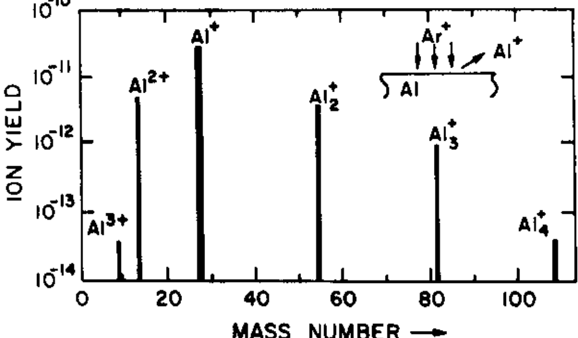

Figure 4.8 Secondary ion cluster spectrum from Ar bombardment of Al. Note that the ordinate is a log scale. The predominant species is Al^+ but Al_2^+ and Al_3^+ are also in abundance. [From Werner, 1978.]

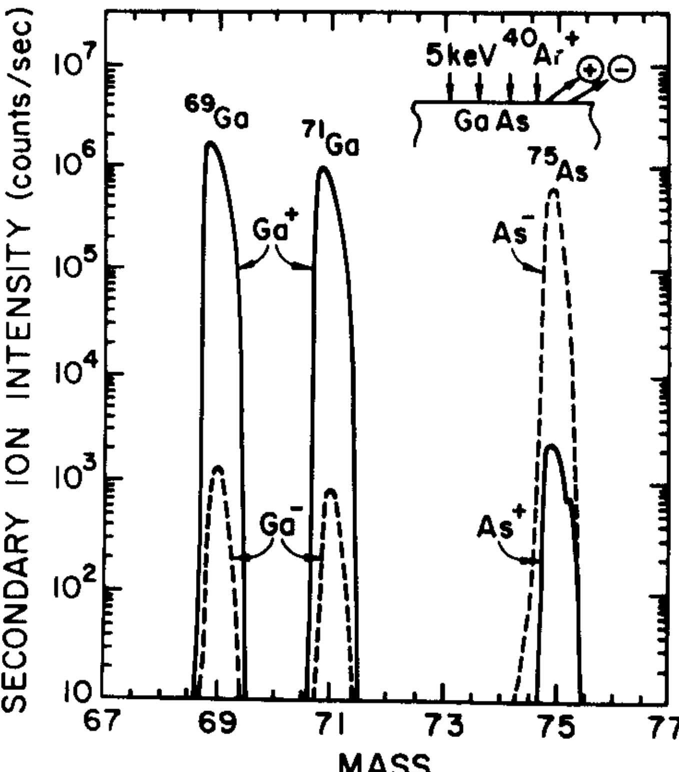

Figure 4.9 Positive (——) and negative (---) ion yields from GaAs bombarded with 5 keV Ar ions. The SIMS spectrum shows the large difference in sensitivity between ionized species for nearly identical sputtering yields of Ga and As from GaAs. [From Magee, *Nucl. Instr. Meth.* **191**, 297 (1981).]

species are emitted as neutrals in various excited states, as ions both positive and negative, singly and multiply charged, and as clusters of particles. The ratio of ionized to neutral species from the same sample can vary by orders of magnitude depending on the condition of the surface. Analysis of sputtered species is the most sensitive of the surface analysis techniques. The common use is the detection and measurement of low concentrations of foreign atoms in solids.

One of the most commonly used sputtering techniques is the collection and analysis of the ionized species—the secondary ions. As shown in Figure 4.7, the secondary ions enter an energy filter, usually an electrostatic analyzer, and then are collected in a mass spectrometer. This gives rise to the acronym SIMS for secondary ion mass spectrometry. All SIMS instruments possess a capability for surface and elemental depth concentration analysis. In one mode of operation the sputter ion beam is rastered across the sample where it

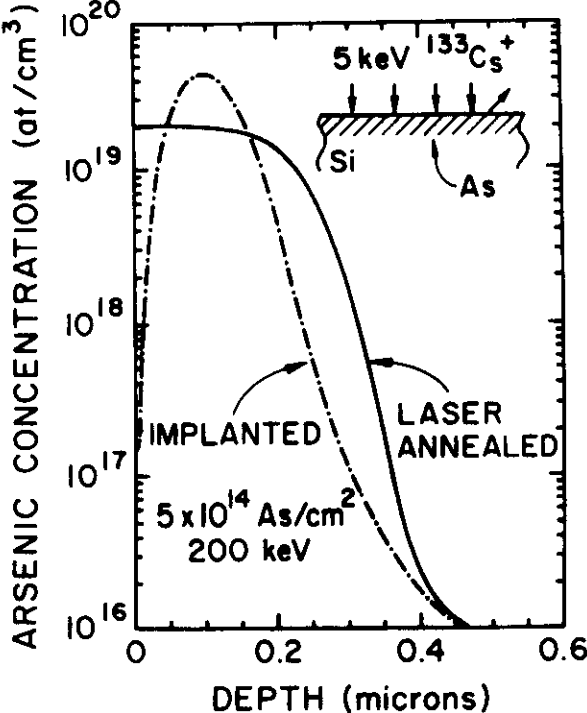

Figure 4.10 SIMS concentration profile of As implanted in Si and redistributed by pulsed laser melting of the outer Si layer. The measured concentration profile extends below levels of $10^{16}/cm^3$. [From C. Magee, RCA Laboratories, private communication.]

erodes a crater in the surface. To insure that ions from the crater walls are not monitored, the detection system is electronically gated for ions from the central portion of the crater. There are also direct imaging instruments—ion microscopes—in which the secondary ions from a defined micro-area of the sample are detected so that an image of the surface composition can be displayed.

The spectra of both positive and negative secondary ions are complex exhibiting not only singly and multiply charged atomic ions but all ionized clusters of target atoms. As shown in Figure 4.8, the mass spectrum from Ar bombarded Al shows not only singly ionized atoms but also doubly and triply ionized atoms and two, three, and four atom clusters. In most cases the yield of singly ionized atoms predominates.

Sputtered particles emerge from the solid with a distribution of energies corresponding to the fluctuations in the many individual events which make up the sputtering process. The sputtered particles have a total yield Y related to the energy spectrum $Y(E)$ such that

$$Y = \int_0^{E_m} Y(E)\, dE, \tag{4.23}$$

where E_m is the maximum energy of the sputtered particles. The positively ionized secondary ion yield $Y^+(E)$ is related to the sputtering yield $Y(E)$ by

$$Y^+(E) = \alpha^+(E) Y(E) \tag{4.24}$$

and the total secondary positive ion yield is

$$Y^+ = \int_0^{E_m} \alpha^+(E) Y(E)\, dE, \tag{4.25}$$

where the ionization probability $\alpha^+(E)$ depends on the particle energy and the nature of the substrate. As shown in Figure 4.9, the ionization yield can vary by three orders of magnitude between species with nearly identical sputtering yields. The major difficulty in quantitative analysis by SIMS is the determination of $\alpha^+(E)$.

The measured signal I^+, generally given in counts/s, of a monoisotopic element of mass A at a concentration C_A in the target is given by

$$I_A^+ = C_A i_p \beta T \alpha^+(E,\theta) Y(E,\theta)\, \Delta\Omega\, \Delta E, \tag{4.26}$$

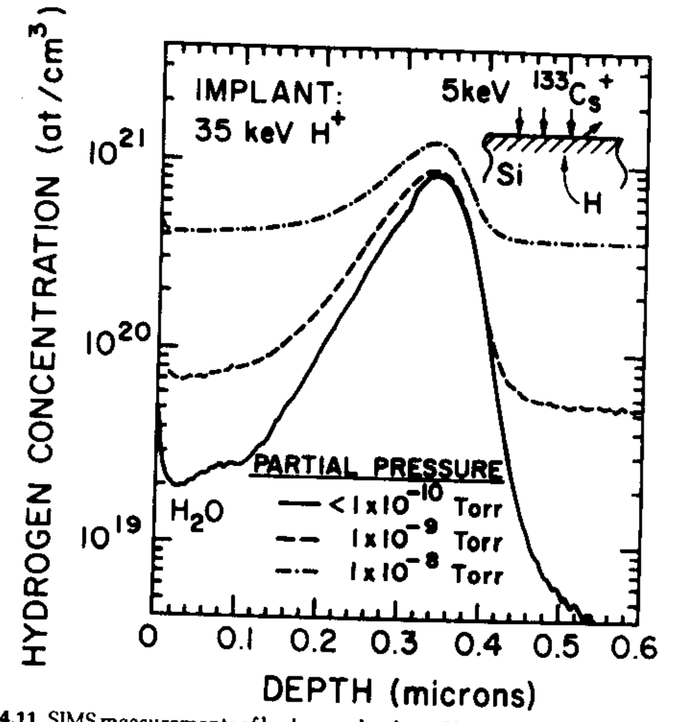

Figure 4.11 SIMS measurements of hydrogen depth profiles for 5 keV Cs sputtering of a silicon sample implanted at 35 keV with a dose of 1×10^{16} H ions/cm^2. The effect of the H_2O partial pressure in the analysis chamber upon the H dynamic range is evident. [From Magee and Botnick, 1981.]

where i_p is the primary beam current (ions/s), θ and E represent the angle and pass energy of the detector system, $\Delta\Omega$ and ΔE are the solid angle and "width" of the energy filter, and β and T are the detector sensitivity and the transmission of the system for the ion species measured. Both α^+ and Y are dependent on the sample composition. The composition dependence can frequently be neglected if concentration profiles of a low level constituent in a matrix of constant composition are to be determined. A good example of this application is measurement of the depth profile of ion implanted impurities in semiconductors (Figure 4.10). The maximum impurity concentration is less than 10^{-3} and hence the presence of the As has minimal effect on α^+. A strong feature of SIMS is the ability to analyze hydrogen over a wide range of concentrations as shown in Figure 4.11. In this case surface contamination by water vapor can influence the dynamic range.

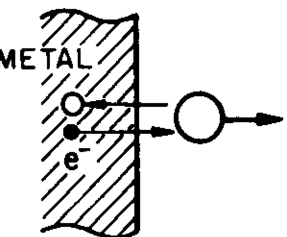

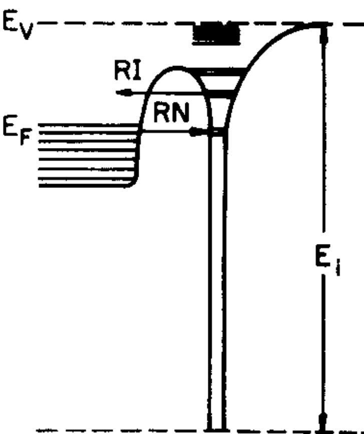

Figure 4.12 Model of the electronic structure of an ion or atom close to a metallic surface. E_F = Fermi energy; E_i = ionization energy; RI = resonance ionization and RN = resonance neutralization.

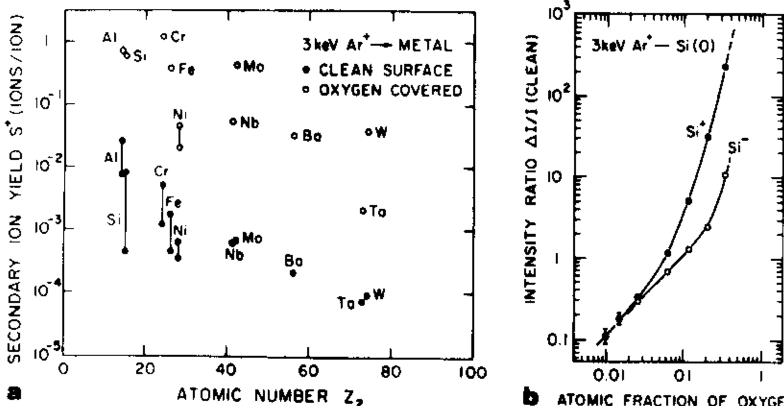

Figure 4.13 (a) Comparison of the secondary ion yield of clean and oxygen covered metals sputtered by 3 keV argon ions. (b) Intensity ratios $\Delta I/I_c$ for Si^+ and Si^- ion yields from oxygen implanted Si versus oxygen concentration for 3 keV Ar sputtered silicon. The oxygen-induced intensity ΔI is given by $\Delta I = I - I_c$, where I is the measured intensity from oxygen-doped Si and I_c is the ion emission from clean Si. (Both (a) and (b) from Wittmaack, *Surface Sci.* **112,** 168 (1981).)

Secondary ion yields are very sensitive to the presence of either electropositive or electronegative ions at the target surface. The picture of neutralization of a positive ion leaving a surface involves the atomic energy levels of the emitted species and the availability of electrons at the solid surface to fill the ionized level. In one view, this process is most efficient when there are electrons in the solid at precisely the same binding energy as the unoccupied level. Under this condition, a resonance tunneling can occur which neutralizes the outgoing species (Figure 4.12). Thus the probability of neutralization depends on the band structure of the solid and the atomic levels of the sputtered ion. For high yields of ionized particles, one desires to reduce the neutralization probability. This could be accomplished by forming a thin oxide layer, which results in a large forbidden gap and a decrease in number of available electrons for neutralization. For example oxygen adsorption causes an enhancement of secondary ion yield. Figure 4.13 shows secondary ion yields for 3 keV Ar bombardment of clean and oxygen-covered metals. The enhancement in yield covers a wide range of two to three orders of magnitude. The enhancement for Si is shown in Figure 4.13b as a function of oxygen concentration in the Si. The sensitivity to an oxidized surface can be an advantage; for this reason, SIMS analysis is often carried out with the surface "flooded" with oxygen or bombarded with an oxygen beam.

4.6 Secondary Neutral Mass Spectrometry (SNMS)

As shown in Figure 4.13 the secondary ion yield from Si could vary over 3 orders of magnitude depending on the oxygen concentration. These matrix effects can be avoided when the sputtered neutral particles are used for composition analysis (Oechsner, 1984). The mass analysis system still requires ions for detection, and, in SNMS, the emission (sputtering) and ionization (charge transfer) processes can be decoupled by ionizing the sputtered neutral atoms after (postionization) emission from the sample surface.

An example of an SNMS system is shown in Figure 4.14, where the major difference from a conventional SIMS system (Figure 4.7) is the insertion of an ionizing plasma chamber in front of the mass spectrometer. The grids act as an electrical diaphragm between the sample and the chamber which prevents ions, of both signs, from

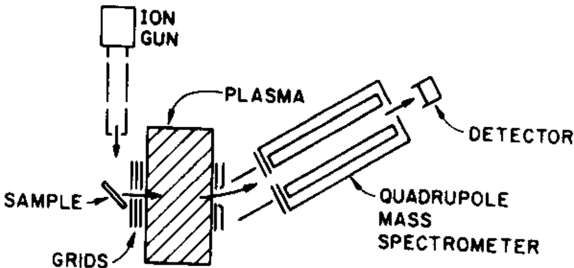

Figure 4.14 Apparatus for carrying out Secondary Neutral Mass Spectrometry (SNMS) in which neutral sputtered species enter a plasma environment for postionization. The ions are then extracted and detected in the quadruple mass spectrometer system.

entering or leaving the chamber. Thus only neutral species enter the ionizing chamber, and species ionized within the chamber cannot reach the sample.

Ionization of the neutral species can be achieved in the chamber by use of a low-pressure high-frequency plasma excited by electron cyclotron wave resonance (Oechsner, 1984). The postionization factor α_A^0 for the sputtered species A depends on the plasma parameters, electron impact ionization of A, and the travel time of A through the ionizer. Values of α_A^0 close to 10^{-1} are achieved for near noble ions and 10^{-2} for transition metal ions like Ta. The postionization factor α^0 is determined by the experimental conditions of the system and for a particular species A, the factor α_A^0 can be treated as a constant for the apparatus.

The measured signal I_A^0 of the neutral species A can be written as

$$I_A^0 = i_p Y_A \alpha_A^0 (1 - \alpha_A^+ - \alpha_A^-) \eta_A^0, \quad (4.27)$$

where i_p is the primary beam current, Y_A is the sputtering yield of A, α_A^+ and α_A^- are ionization yields for the formation of secondary ions, and η_A is the instrumental factor. The ionization probabilities α^+ and α^- are usually well below unity so the factor $(1 - \alpha^+ - \alpha^-)$ can be treated as unity. Since sample matrix effects are small in the postionization factor α^0, calibration can be achieved readily by use of standards. The sensitivity of SNMS to low concentrations of impurities is comparable to that of SIMS with a detection value of about 1 ppm. In SNMS, however, one does not expect large variations in yield with variation in the properties of the substrate. Instead of plasmas, high powered lasers can be used to ionize the neutral species.

4.7 Preferential Sputtering and Depth Profiles

In a description of sputtering from a multicomponent system, the influence of preferential sputtering and surface segregation must be included. For a homogeneous sample with two atomic components A and B, the surface concentrations C^s are equal to those in the bulk, C^b, in the absence of segregation to the surface which might occur due to thermal processes. Then at the start of sputtering

$$C_A^s / C_B^s = C_A^b / C_B^b. \quad (4.28)$$

The partial yield of atomic species A and B is defined as in Eq. (4.1) by

$$Y_{A,B} = \frac{\text{Number of ejected atoms A,B}}{\text{Incident particle}}. \quad (4.29)$$

The partial sputtering yield Y_A of species A is proportional to the surface concentration C_A^s and similarly Y_B is proportional to C_B^s. The ratio of partial yields is given by

$$\frac{Y_A}{Y_B} = f_{AB} \cdot \frac{C_A^s}{C_B^s}, \quad (4.30)$$

where the sputtering factor f_{AB} takes into account differences in surface binding energies, sputter escape depths, and energy transfers within the cascade. Measured values of f_{AB} generally are in the range between 0.5 and 2.

In the case where f_{AB} is unity, $Y_A / Y_B = C_A^s / C_B^s$ and the yield of sputtered particles is a direct measure of the bulk concentration ratio. In the case where $f_{AB} \neq 1$, the surface concentrations and yields will change from their initial values, $C_A^s(0)$ and $Y_A(0)$, to their values, $C_A^s(\infty)$ and $Y_A(\infty)$, at long times when steady state is achieved.

At the start of sputtering, $t = 0$,

$$\frac{Y_A(0)}{Y_B(0)} = f_{AB} \cdot \frac{C_A^s(0)}{C_B^s(0)} = f_{AB} \cdot \frac{C_A^b}{C_B^b}. \quad (4.31)$$

At long times, when steady state conditions have been achieved, conservation of mass requires that the ratios of partial yields equal the bulk concentration ratio,

$$\frac{Y_A(\infty)}{Y_B(\infty)} = \frac{C_A^b}{C_B^b}. \quad (4.32)$$

For example, if there is preferential sputtering where $f_{AB} > 1$, the sputtering yield of A is greater than that of B, and the surface will be enriched in B. This enrichment of the surface produces an increase in

the sputtering yield of B (more B atoms) and a decrease in the sputtering yield of A (less A atoms). As the process continues with macroscopic amounts (greater than 100 Å) of material removed, the increased concentration of B just balances out the preferential sputtering of A. Therefore, at steady state the surface concentration ratio will differ from that of the bulk when $f_{AB} \neq 1$:

$$\frac{C_A^s(\infty)}{C_B^s(\infty)} = \frac{1}{f_{AB}} \cdot \frac{C_A^b}{C_B^b}. \tag{4.33}$$

That is, the surface composition is rearranged so that the total sputtering yield gives the bulk composition in spite of differences in yields of the individual atomic species. Analysis of the composition of the remaining surface layer at this point would show a difference from that of the bulk composition.

An example of the change in composition of a silicide layer is shown in Figure 4.15 for PtSi that was sputtered with 20 keV argon ions and then analyzed with 2 MeV ^{4}He ions. The Rutherford backscattering spectrum shows an enrichment of the Pt concentration in the surface region. The ratio of Pt/Si increased from the value of unity associated with that of the bulk values to a value near two in the surface region. The increase in the Pt concentration is due to the fact

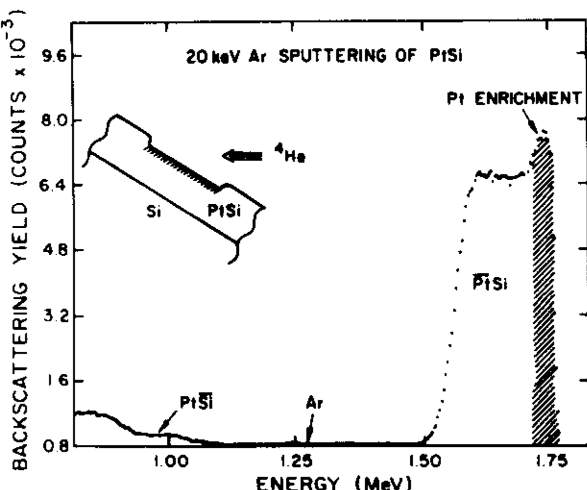

Figure 4.15 RBS spectrum of a PtSi film after sputtering with 20 keV Ar ions. The shaded portion in this Pt signal indicates an increase in the concentration of Pt in the near surface region as a result of the enhanced Si sputtering. [From Liau et al., *J. Appl. Phys.* **49**, 5295 (1978).]

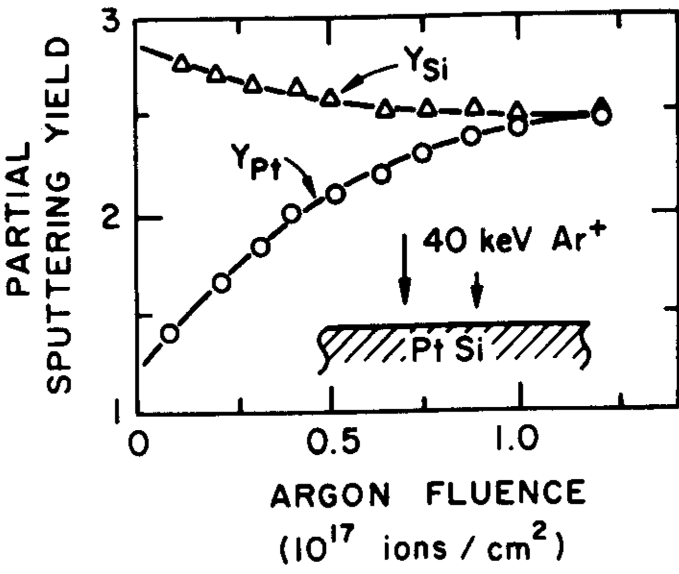

Figure 4.16 Dose dependence of the partial sputtering yields of Si and Pt emitted from PtSi for 40 keV Ar bombardment. [From Liau and Mayer, 1980.]

that the partial sputtering yield of Si is greater than that of Pt, $Y_{Si} > Y_{Pt}$. Figure 4.16 shows the partial yields as a function of argon ion dose. As one would expect, at low bombardment doses the sputtering yield of Si is significantly greater than that of Pt. At the onset of sputtering the yield ratio $Y_{Si}(0)/Y_{Pt}(0) = 2.4$. As the bombardment proceeds, the partial sputtering yields merge into the same value. The equality of the Si and Pt yields merely reflects the fact that the yield ratio after steady state has been reached is equal to the bulk concentration ratio which for PtSi is unity.

4.8 Interface Broadening and Ion Mixing

One of the applications of sputtering is the removal of deposited or grown layers in thin film structures in order to analyze the composition at the interface between the film and substrate. In these applications, the penetration of the ions used in the sputtering beam can induce an intermixing between the film and substrate due to the strong atomic displacements and diffusion that occurs within the collision cascade around the track of the ion used in sputtering. This

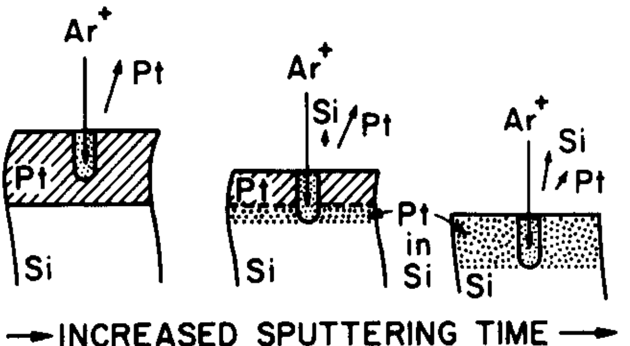

Figure 4.17 Schematic diagram of Ar sputtering of a 1000 Å Pt layer on Si at three different times in the sputtering process. When the Ar range is less than the Pt film thickness, only Pt ions are sputtered. When the Ar ion penetrates through the Pt/Si interface, ion-induced intermixing occurs and a Si signal is found in the sputtering yield. After the initial Pt film has been removed, a Pt signal is still observed due to mixing of Pt into the substrate Si. [From Liau et al., *J. Vac. Sci. Technol.* **16**, 121 (1979).]

intermixing leads to an artificial broadening of the concentration depth profiles at the interface.

Sputtering requires bombardment of the surface with primary ions of appreciable energy (typically 1–20 keV) whose range far exceeds the escape depth of the sputtered ions and often exceeds the observation depth in electron spectroscopies. Therefore, due to the ion-induced intermixing in the collision cascade, a zone of altered material precedes the "analytical" zone during layer removal. Ion mixing is illustrated in Figure 4.17 for SIMS analysis of a Pt film deposited on Si and sputtered by argon ions. When the argon ions penetrate through the Pt/Si interface some of the Si atoms in the substrate will be transported to the top surface of the Pt film where they can be sputtered. Thus a silicon signal will appear before the Pt film is sputtered away. Platinum is also intermixed with the Si, and, consequently, a Pt signal will persist in the SIMS spectrum at depths well beyond the thickness of the original deposited layer of Pt.

An estimate of the interfacial broadening in such systems can be made by setting the range R of the sputtering ion equal to the half-width of the broadened signal. The ion range is given by

$$R = \int_{E_0}^{0} \frac{1}{dE/dx}\, dE, \qquad (4.34)$$

which can be approximated for medium mass ions in the keV energy range by assuming that nuclear energy loss dominates and has an energy independent value,

$$R = E_0/(dE/dx)_n, \qquad (4.35)$$

where $(dE/dx)_n$ is given by Eq. (4.19). The value of $(dE/dx)_n$ for Ar ions in Cu is about 100 eV/Å, which is the basis for the rule of thumb that the altered layer extends 10 Å/keV.

The amount of interface broadening can be minimized by proper choice of ion energies and incident angles during sputter profiling. In many cases, sputter depth profiles can have a better depth resolution than that obtained with backscattering spectrometry.

When possible it is advantageous to use two or more analytical techniques that provide complementary data. Figure 4.18 shows the analysis of a tungsten silicide film on polycrystalline silicon (polySi). Secondary ion mass spectroscopy (Figure 4.18a) is used to determine the phosphorus concentration in polySi and to detect oxygen contamination at the interface. Backscattering spectrometry (Figure 4.18b) provides the depth scale and the composition of the sputter deposited silicide—in this case 1830 Å of $WSi_{2.7}$. In the SIMS data the phosphorus concentration in polySi was calibrated from a standard obtained by implanting phosphorus into a silicon sample.

The ratio of W to Si signals in SIMS data (Figure 4.18a) does not reflect the silicide composition, and there is an order of magnitude increase in the Si signal going from the silicide into the Si. These effects are due to the influence of the matrix on the yield of secondary ions. The peak in the W signal at the silicide/Si interface is due to the enhancement of the W ion yield because of oxygen at the interface (note also the enhancement of the phosphorus yield at the Si/SiO_2 interface). The RBS spectrum (Figure 4.18b) shows that there is no peak in the W distribution at the interface and that the composition of the silicide is $WSI_{2.7}$. The increase in the Si signal around 950 keV is due to the increase in Si concentration going from silicide to Si and the decrease around 800 keV is due to the presence of a 700 Å thick layer of SiO_2 at the interface between the polySi layer and substrate Si. The signal from the 1 atom % of phosphorus in the polySi cannot be detected in the RBS spectrum but is easily detected in the SIMS data. The amount of interface broadening is minimal in the depth profile of the SIMS data and the concentration of light mass elements (oxygen and phosphorus) can easily be detected. The strong influence of the matrix on the ion yield does not allow an accurate determination of the relative concentration of the major constituents (tungsten and

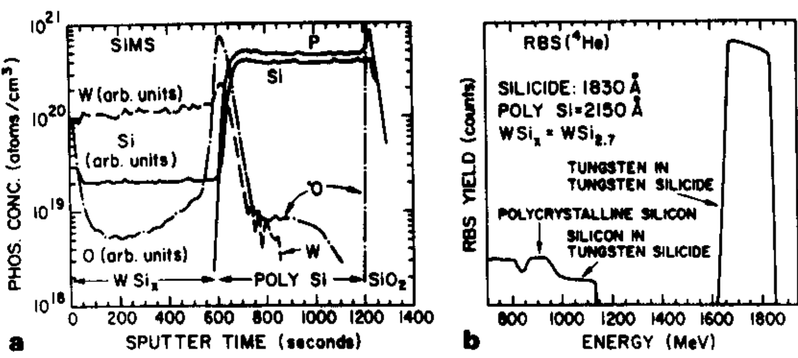

Figure 4.18 (a) Secondary ion mass spectroscopy (SIMS) and (b) Rutherford backscattering spectrometry (RBS) analysis of a tungsten silicide layer sputter deposited on a phosphorus-doped polycrystalline silicon layer on a layer of SiO_2 on silicon. [Data from C. Magee, RCA Research Laboratories, private communication.]

silicon); these quantities are found along with layer thicknesses from the Rutherford backscattering spectrum. By the use of two complementary analytical techniques (RBS and SIMS) a rather accurate picture of the composition of the sample can be obtained.

4.9 Thomas–Fermi Statistical Model of the Atom

In low-velocity collisions the impact parameter is sufficiently large so that the nuclear charge is screened by the electrons. This leads to a modification of the scattering potential from that of the unscreened Coulomb potential, $V = Z_1Z_2e^2/r$. The modified potential is found from the Thomas–Fermi description which treats all atoms as identical aside from scaling factors.

The Thomas–Fermi model assumes that the electrons can then be treated by statistical mechanics, Fermi–Dirac statistics, in which they behave as an ideal gas of particles which fills the potential well around the positively charged core. The density of states, $n(E)$, of a free electron gas is obtained by applying periodic boundary conditions and box normalization to a cell of length L to give

$$n(E) = \frac{L^3}{2\pi^2\hbar^3}(2m)^{3/2}E^{1/2}. \qquad (4.36)$$

The energy of the gas increases as the number of electrons increases. For a collection of electrons, the number at a point r, $Z(r)$, is given by

$$Z(r) = \int_0^{E_F(r)} n(E)\,dE = \frac{L^3(2m)^{3/2}}{2\pi^2\hbar^3}\int_0^{E_F(r)} E^{1/2}\,dE = \frac{L^3(2m)^{3/2}}{3\pi^2\hbar^3}E_F(r)^{3/2}, \qquad (4.37)$$

where $E_F(r)$ is associated with the maximum energy of the ensemble of electrons at r.

The Fermi energy is simply the energy of the highest filled state. In the many-electron atom which we are treating, the total energy E_r of an electron is $E_r = E_K + V(r)$, where E_K is the kinetic energy. For a bound electron $E_r \leq 0$ which requires that for the maximum kinetic energy electron $E_F = -V(r)$. From Eq. (4.37)

$$\rho(r) = \frac{Z(r)}{L^3} = \frac{(2m)^{3/2}}{3\pi^2\hbar^3}[-V(r)]^{3/2}. \qquad (4.38)$$

The self-consistency condition is that the potential due to the electron density in Eq. (4.38), as well as that due to the nuclear charge, properly reproduce the potential energy, $-V(r)$. Consequently, the charge density, $-e\rho$, and the electrostatic potential, $-[V(r)/e]$, must satisfy Poisson's equation

$$-\frac{1}{e}\nabla^2V = -4\pi(-e\rho),$$

or

$$\nabla^2V = \frac{1}{r^2}\frac{d}{dr}\left(r^2\frac{dV}{dr}\right) = 4\pi e^2\rho = \frac{4e^2[-2mV(r)]^{3/2}}{3\pi\hbar^3}. \qquad (4.39)$$

Equations (4.38) and (4.39) may be solved simultaneously for ρ and V, with the boundary conditions: As $r \to 0$, the leading term in the potential energy must be due to the nucleus, so that $V(r) \to -Ze^2/r$, and as $r \to \infty$, there must be no net charge inside the sphere of radius r, so that V falls off more rapidly than $1/r$, and $rV(r) \to 0$.

Equation (4.39) and the boundary conditions given above are conveniently expressed in a dimensionless form in which Z, E, m, and h appear only in scale factors. We put

$$V(r) = -\frac{Ze^2}{r}\chi, \quad r = ax$$

and

$$a = \frac{1}{2}\left(\frac{3\pi}{4}\right)^{2/3}\frac{\hbar^2}{me^2Z^{1/3}} = \frac{0.885a_0}{Z^{1/3}}, \qquad (4.40)$$

where $a_0 = \hbar^2/me^2$, the Bohr radius. Equation (4.8) indicates that the scaling parameter to describe the size of an atom is inversely proportional to the cube root of the atomic number. (For electron spectroscopies where transitions are between core levels the 1s radius is approximated by a_0/Z.) With these substitutions, Eq. (4.39) becomes

$$x^{1/2}\frac{d^2\chi}{dx^2} = \chi^{3/2}. \tag{4.41}$$

In this dimensionless Thomas-Fermi (TF) equation, the potential behaves like a simple Coulomb interaction in the extreme case as $r \to 0$. The accurate solution of Equation (4.41) is carried out numerically and there are also analytical approximations represented in series expansions or exponentials. The Molière approximation to the Thomas-Fermi screening function shown in Figure 4.4 is most often used in computer simulations and is given by

$$\chi(x) = 0.35e^{-0.3x} + 0.55e^{-1.2x} + 0.10e^{-6.0x}, \tag{4.42}$$

where $x = r/a$.

Problems

4.1. The maximum value of the nuclear energy loss occurs at reduced energy value of 0.3 for the Thomas-Fermi potential. What energy in keV does $\epsilon' = 0.3$ correspond to for Ar incident on Si, oxygen on Si?

4.2. Assuming nuclear energy loss dominates and the stopping cross section is energy independent, what is the range of 10 keV Ar ions incident on Cu.

4.3. For a screened Coulomb collision with $\chi = a/2r$ use the impulse approximation to show that b, the impact parameter, is proportional to $(a/E\theta)^{1/2}$ and derive $\sigma(\theta)$, the cross section.

4.4. Calculate the ratio of the unscreened to screened nuclear cross section $d\sigma/dT$ for the following cases: 2.0 MeV He^+ on Au, 0.1 MeV He^+ on Au, and 1 KeV Ar on Cu.

4.5. For a scattering potential $V(r) \propto r^{-3}$, what is the energy dependence of the energy loss dE/dx.

4.6. Calculate the sputtering yield for 45 keV Ar ions incident on Si ($U_0 = 4.5$ eV) using a screened potential. Compare your answer with the data given in Figure 4.2.

4.7. If the sputtering yield of species A is twice that of species B in a matrix AB, what is the ratio A to B of the flux of sputtered species at (a) the initial time and (b) the steady state time and what is the ratio A to B of surface composition at (c) the initial time and (d) the steady state time?

4.8. Determine the time in seconds required to sputter 500 Å of Si using a 10μA/cm^2 beam of 45 keV ions of (a) Ne, (b) Kr, and (c) Xe. (Use data given by the solid line in Figure 4.2.)

References

1. E. E. Anderson, *Modern Physics and Quantum Mechanics* (W. B. Saunders Co., Philadelphia, 1971).
2. H. H. Andersen and H. L. Bay, "Sputtering Yield Measurements," in *Sputtering by Particle Bombardment I*, R. Behrisch, Ed. (Springer-Verlag, New York, 1981), Chapter 4.
3. R. Behrisch, Ed., *Sputtering by Particle Bombardment I and II* (Springer-Verlag, New York, 1981 and 1983).
4. G. Carter and J. S. Colligon, *Ion Bombardment of Solids* (Elsevier Science Publishing Co., New York, 1968).
5. G. Carter, B. Narvinsek, and J. L. Whitton, Heavy Ion Sputtering Induced Surface Topography Development," in *Sputtering by Particle Bombardment II*, R. Behrisch, Ed. (Springer-Verlag, New York, 1983).
6. W. K. Chu, "Energy Loss of High Velocity Ions in Matter," in *Atomic Physics*, P. Richard, Ed., Methods of Experimental Physics, Vol. 17 (Academic Press, New York, 1980), Chapter 2.
7. Z. L. Liau and J. W. Mayer, "Ion Bombardment Effects on Material Composition," in *Ion Implantation*, J. K. Hirvonen, Ed., Treatise on Materials Science and Technology, Vol. 18, N. Herman, Ed. (Academic Press, New York, 1980), Chapter 2.
8. J. Lindhard, M. Scharff, and H. E. Schiott, Range Concepts and Heavy Ion Ranges (Notes on Atomic Collision, II), *Mat. Fys. Medd. Dan. Vid. Selsk.* 33(14), (1963).
9. C. Magee and E. M. Botnick, *J. Vac. Sci. Technol.* 19(47) (1981).
10. J. A. McHugh, "Secondary Ion Mass Spectrometry," in *Methods of Surface Analysis*, A. W. Czanderna, Ed. (Elsevier Science Publishing Co., New York, 1975), Chapter 6.
11. J. M. McCrea, "Mass Spectrometry," in *Characterization of Solid Surfaces*, P. F. Kane and G. B. Larrabee, Eds. (Plenum Press, New York, 1974), Chapter 2.

12. H. Oechsner, Ed., *Thin Film and Depth Profile Analysis* (Springer-Verlag, New York, 1984).
13. P. Sigmund, "Sputtering Processes: Collision Cascades and Spikes," in *Inelastic Ion-Surface Collisions*, N. Tolk et al., Eds. (Academic Press, New York, 1977), pp. 121–152.
14. P. Sigmund, "Sputtering by Ion Bombardment; Theoretical Concepts," in *Sputtering by Particle Bombardment I*, R. Behrisch, Ed. (Springer-Verlag, New York, 1981), Chapter 2.
15. I. M. Torrens, *Interatomic Potentials* (Academic Press, New York, 1972).
16. P. D. Townsend, J. C. Kelley, and N. E. W. Hartley, *Ion Implantation, Sputtering and Their Applications* (Academic Press, New York, 1976).
17. H. W. Werner, "Introduction to Secondary Ion Mass Spectrometry (SIMS)," in *Electron and Ion Spectroscopy of Solids*, L. F. Ermans et al., Eds. (Plenum Press, New York, 1978).

CHAPTER

11 NONRADIATIVE TRANSITIONS AND AUGER ELECTRON SPECTROSCOPY

11.1 Introduction

In previous chapters, we have discussed inner shell vacancy formation by photon irradiation (the basis of X-ray photoelectron spectroscopy) or energetic electron and proton irradiation. The excited atoms can release their energy in radiative transitions (Chapter 10) with the emission of X-rays or in nonradiative transitions with the emission of electrons. The latter process forms the basis for Auger electron spectroscopy (AES) in which one determines composition by measuring the energy distribution of electrons emitted during irradiation with a beam of energetic electrons. As with other electron spectroscopies, the observation depth is about 10–30 Å and is determined by the escape depth (Chapter 6). The identification of atoms by core level spectroscopies is based upon the values of the binding energies of the electrons. With Auger electron spectroscopy, the energy of the emergent electron is determined by the differences in binding energies associated with the deexcitation of an atom as it rearranges its electron shells and emits electrons (Auger electrons) with characteristic energies. Figure 11.1 shows the Auger radiationless deexcitation processes, in which the atom is left in the final state with two vacancies (or holes). If one of the final state vacancies lies in the same shell as the primary vacancy (although not in the same subshell), the radiationless transition is referred to as a Coster–Kronig transition. This transition is significant because the Coster–Kronig transition rates are

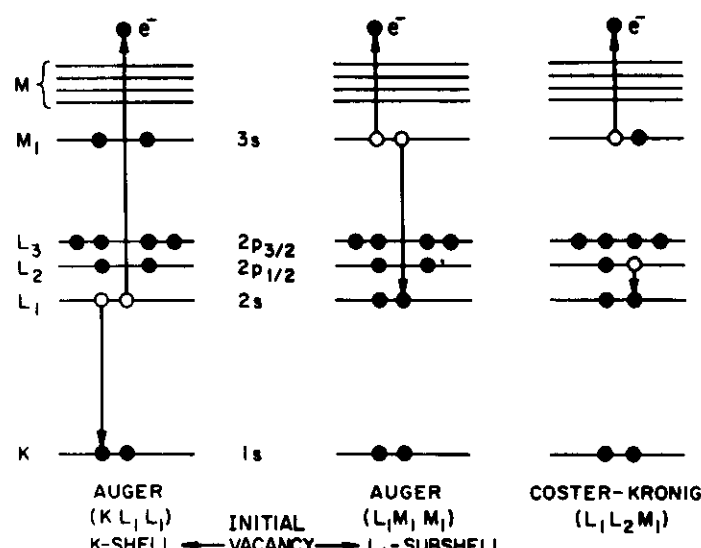

Figure 11.1 Schematic diagram of various two-electron deexcitation processes. The KL_1L_1 Auger transition corresponds to an initial K hole which is filled with an L_1 electron and simultaneously the other L_1 electron is ejected to the vacuum. The LM_1M_1 Auger transition is the corresponding process with an initial 2s vacancy. The Coster–Kronig $L_1L_2M_1$ transition contains an initial L_1 hole which is filled with an electron from the same shell (but different subshell, L_2).

much higher than the normal Auger transitions and influence the relative intensities of the Auger lines. For example in Figure 11.1, if an L_1 shell has a vacancy, the L_2 to L_1 transition will be rapid (Coster–Kronig), therefore reducing M electron to L_1 vacancy transitions.

11.2 Auger Transitions

11.2.1 Nomenclature

The nomenclature used to describe the Auger processes is shown in Figure 11.1. For vacancies in the K shell, the Auger process is initiated when an outer electron such as an L_1 electron (dipole selection rules are not followed) fills the hole. The energy released can be given to another electron such as another L_1 or an L_3 electron which is then ejected from the atom. The energy of the outgoing electron is $E_K - E_{L_1} - E_{L_1}$. The process described is called a KLL Auger transition in general terms and, more specifically denoted as KL_1L_1 or KL_1L_3. If there are vacancies in the L shell, one can have Auger processes in

which an electron from the M shell (M_1 electron) fills the L hole and another M shell electron (for example, an M_1 electron) is ejected, an $L_1M_1M_1$ Auger transition. Since electron–electron interactions are strongest between electrons whose orbitals are closest together, the strongest Auger transitions are of the type KLL or LMM. For Coster–Kronig transitions the vacancy is filled by electrons which come from the same shell, i.e., LLM. Auger transitions involving the outermost orbitals, the valence band, have an energy width of about twice that of the valence band. In Figure 11.2, the Si $KL_1L_{2,3}$ and $L_{2,3}V_1V_2$ (or LVV) Auger transitions are indicated with V_1 and V_2 located at positions of maxima in the density of states in the valence band.

A complete nomenclature describing Auger transitions indicates the shells involved and the final state of the atom. The final state is usually described using the spectroscopic notation describing the orbitals. For example, a KL_1L_1 transition would leave the 2s shell empty (two vacancies) and the 2p shell with six electrons; the transition is KL_1L_1 $(2s^02p^6)$. A KL_2L_3 would leave the vacancies in the 2p shell and would be indicated KL_2L_3 $(2s^22p^4)$. Even in the relatively simple KLL transition, there are a large variety of final states which can have slightly different energies and hence correspond to slightly different Auger lines. In the following we discuss this in detail.

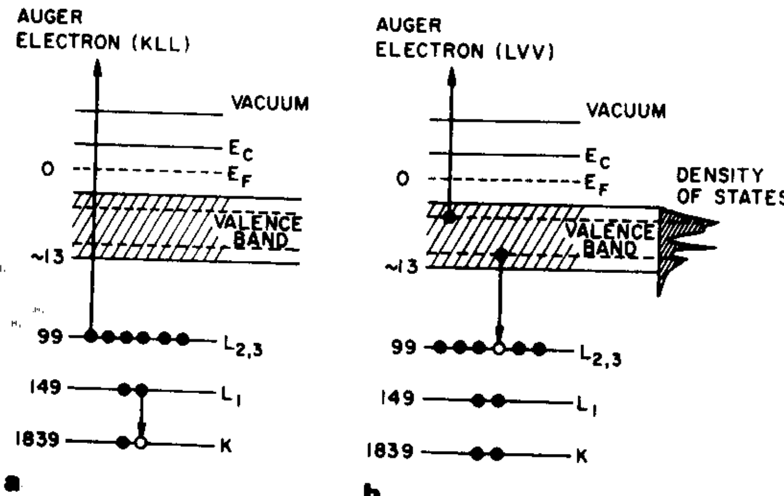

Figure 11.2 Schematic of the (a) $KL_1L_{2,3}$ and (b) LVV Auger deexcitation processes in Si. Binding energies are indicated on the left. The energy of Auger electron in the $KL_1L_{2,3}$ process is approximately 1591 eV and the $L_{2,3}VV$ Auger electron has an energy of approximately 90 eV.

11.2.1.1 KL_1L_1

In the usual X-ray notation this transition corresponds to an initial state of a single 1s hole and a final state of two 2s holes. We can consider electron holes as electrons to find the possible final configurations of the final states. The n = 2 shell is now considered as $2s^0 2p^6$ (where the filled shell is $2s^2 2p^6$) and has states given by the possible allowed quantum numbers consistent with the Pauli exclusion principle: $m_s = \pm 1$, $M_L = 0$, $M_s = 0$, where M_L and M_s are the total orbital and spin angular momenta, respectively. The notation ^1S indicates a state of total orbital momentum zero (S). This transition is properly written $KL_1L_1(^1S)$, although the final state (^1S) is the only one allowed and, in this case, the notation is slightly redundant.

11.2.1.2 KL_1L_2 or KL_1L_3

In this case the final state electron configuration is written $2s^1 2p^5$. The possible quantum states are ^1P and ^3P, where P denotes the total orbital angular momentum. This corresponds to two states coupling to total angular momentum L = 1, i.e., a P state with the electron spins aligned ^3P and antialigned ^1P.

11.2.1.3 KL_2L_2; KL_2L_3; KL_3L_3 Transitions

Here the final states can couple to total angular momenta states of D(L = 2), P(L = 1), and S(L = 0) with different possible spin alignments to yield states ^1D, ^3P, and ^1S.

Thus in KLL type of transitions there are a total of six final states possible:

$KL_1L_1 — 2s^0 2p^6(^1S)$,
$KL_1,L_{2,3} — 2s^1 2p^5(^1P,^3P)$,
$KL_{2,3},L_{2,3} — 2s^2 2p^4(^1D,^3P,^1S)$.

These final states are shown experimentally in Figure 11.3 for the case of magnesium. [Actually the $2s^2 2p^4(^3P)$ state is not observed due to lack of intensity.]

11.2.2 Energies

The energy of the Auger electrons can in principle be determined in the same way as that of X-rays: by the difference of the total energies before and after the transition. An empirical way of doing that, for example, is by

$$E^Z_{\alpha\beta\gamma} = E^Z_\alpha - E^Z_\beta - E^Z_\gamma - \tfrac{1}{2}(E^{Z+1}_\gamma - E^Z_\gamma + E^{Z+1}_\beta - E^Z_\beta), \tag{11.1}$$

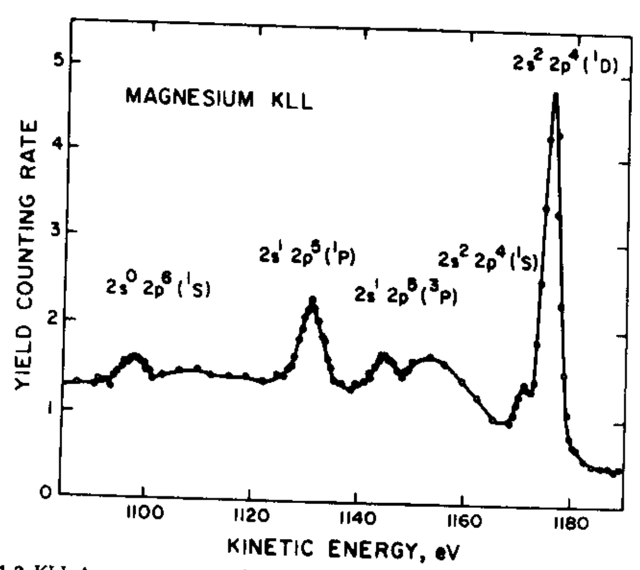

Figure 11.3 KLL Auger spectrum of magnesium containing 5 of the 6 lines predicted in L–S coupling. [From Siegbahn et al., 1967.]

where $E^Z_{\alpha\beta\gamma}$ is the Auger energy of the transition $\alpha\beta\gamma$ of the element Z. The first three terms correspond to the difference in the binding energies of shells α, β, γ of the element Z. The correction term is small and involves the average of the increase in binding energy of the γ-electron when a β-electron is removed and of the β-electron when a γ-electron is removed. Measured values of Auger KLL transitions are given in the Appendices along with values of the binding energies. A

Table 11.1 Tabulation of Values Used to Calculate the Energy of the KL_1L_2 Auger Transition in Ni

(1) $E^{Ni}_{KL_1L_2} = E^{Ni}_K - E^{Ni}_{L_1} - E^{Ni}_{L_2} - \tfrac{1}{2}(E^{Cu}_{L_2} - E^{Ni}_{L_2} + E^{Cu}_{L_1} - E^{Ni}_{L_1})$

(2) Electron binding energies in keV from Appendix 5

$E^{Ni}_K = 8.333$	$E^{Cu}_{L_2} = 0.951$	$E^{Cu}_{L_1} = 1.096$
$-E^{Ni}_{L_1} = 1.008$	$-E^{Ni}_{L_2} = \underline{0.872}$	$-E^{Ni}_{L_1} = \underline{1.008}$
$-E^{Ni}_{L_2} = \underline{0.872}$	0.079	0.088
6.453	$\tfrac{1}{2}(0.079 + 0.088) = 0.084$	

$E^{Ni}_{KL_1L_2} = 6.453 - 0.084 = 6.369$ keV

(3) Auger transition energy from Appendix 7

$E^{Ni}_{KL_1L_2} = 6.384$ keV

Figure 11.4 Principal Auger electron energies versus atomic number. The heavy points indicate the strong transitions for each element. [From Davis et al., 1976.]

numerical test of the approximation of Eq. (11.1) is given in Table 11.1 for KLL transitions. The agreement is good. Figure 11.4 shows the dominant Auger energies versus atomic number. The strong Z dependence of the binding energies leads to a straightforward elemental identification using this technique.

11.2.3 Chemical Shifts

The chemical environment of an atom is reflected in changes in the valence shell orbitals which in turn influence the atomic potential and the binding energy of the core electrons. The binding energies of the inner core K and L shells shift in unison with changes in the chemical environment. For this reason, the K_α X-ray emission lines, which are transitions between K and L shells, have only small shifts. For KLL Auger electron lines both the K and L shells are involved, but unlike the K_α X-ray emission lines, the L shell is involved twice in the transition. The inner shell electron that is ejected in KLL Auger processes therefore will display a chemical shift. Thus, one would expect chemical shifts in both AES and XPS spectra.

Chemical shifts are evident in both AES and XPS spectra. However, the chemical shifts are more difficult to interpret in the two electron Auger process than in the one electron photoelectric process. Further, Auger linewidths are broader than XPS lines. Consequently, the latter technique is typically used to explore changes in chemical binding.

11.2.4 Estimate of the Auger Transition Probability in a Hydrogenlike Atom: KLL Transition

In the usual manner the transition probability for the Auger effect, W_A, can be written as

$$W_A = \frac{2\pi}{\hbar}\rho(k)\left|\phi_f(\mathbf{r}_1)\psi_f(\mathbf{r}_2)\frac{e^2}{|\mathbf{r}_1 - \mathbf{r}_2|}\phi_i(\mathbf{r}_1)\psi_i(\mathbf{r}_2)\, d\mathbf{r}_1\, d\mathbf{r}_2\right|^2, \quad (11.2)$$

where $\rho(k) = m\,(V/8\pi^3\hbar^2)\,k \sin\theta\, d\theta d\phi$ is the density of states associated with normalization in a box of volume V and for a KLL Auger transition from a hydrogenlike atom:

$$\phi_i(\mathbf{r}_1) = \frac{1}{\sqrt{6a^3}}\frac{\mathbf{r}_1}{a}\, e^{-\mathbf{r}_1/2a} Y_1^m(\theta_1, \phi_1), \quad (11.3)$$

$$\phi_f(\mathbf{r}_1) = \frac{2}{\sqrt{a^3}}\, e^{-\mathbf{r}_1/a}, \quad (11.4)$$

$$\psi_i(\mathbf{r}_2) = \frac{1}{\sqrt{6a^3}}\frac{\mathbf{r}_2}{a}\, e^{-\mathbf{r}_2/2a} Y_1^m(\theta_2, \phi_2), \quad (11.5)$$

$$\psi_f(\mathbf{r}_2) = \frac{1}{\sqrt{V}}\, e^{i\mathbf{k}\cdot\mathbf{r}_2}. \quad (11.6)$$

These wave functions represent electrons in the 2p state, the 1s state, the 2p state, and a free electron, respectively, with $a = a_0/Z$ and a_0 is the Bohr radius. For convenience it is useful to write these equations as functions of $\mathbf{r}/a$:

$$\phi_i(\mathbf{r}_1) = \frac{1}{\sqrt{6a^3}}\,\phi_i'\left(\frac{\mathbf{r}_1}{a}\right), \quad (11.3')$$

$$\phi_f(\mathbf{r}_1) = \frac{2}{\sqrt{a^3}}\,\phi_f'\left(\frac{\mathbf{r}_1}{a}\right), \quad (11.4')$$

$$\psi_i(\mathbf{r}_2) = \frac{1}{\sqrt{6a^3}}\,\psi_i'\left(\frac{\mathbf{r}_2}{a}\right), \quad (11.5')$$

$$\psi_f(\mathbf{r}_2) = \frac{1}{\sqrt{V}}\, e^{ia\mathbf{k}\cdot\mathbf{r}_2/a} \quad (11.6')$$

and the potential as

$$\frac{e^2}{a}\left(\frac{1}{|\mathbf{r}_1/a - \mathbf{r}_2/a|}\right) = \frac{e^2}{a} V'(\mathbf{r}_1/a, \mathbf{r}_2/a). \qquad (11.7)$$

In this calculation we are considering a KL_2L_2 Auger transition, the transition of a 2p electron (L_2) to the 1s state (K) and the subsequent emission of another 2p electron (L_2) to a free electron. In this hydrogenic model the energy of the Auger electron, E_A, is

$$E_A = E_K - E_L - E_L = E_K/2,$$

where E_K and E_L are the binding energies of the K and L shells, respectively, and $E_L = \frac{1}{4} E_K$ in the Bohr model. In the hydrogenic model

$$E_K = e^2Z^2/2a_0$$

and

$$a = a_0/Z$$

so that

$$ak = (a_0/Z)\sqrt{mE_K/\hbar^2},$$
$$= 1/\sqrt{2},$$

where we have used the Bohr relation $a_0 = \hbar^2/me^2$. Then

$$\psi_f(\mathbf{r}_2) = \frac{1}{\sqrt{V}} e^{i r_2 \cos\theta_2/a\sqrt{2}}.$$

In this form we can extract the basic dependence of the transition probability on atomic parameters such as the atomic number Z. Substituting (11.3)–(11.7) (in modified form) into the formula for the transition probability, we find

$$W_A = \frac{2\pi}{\hbar}\frac{mk\,d\Omega}{\hbar^2 8\pi^3}\frac{e^4 a}{9} F, \qquad (11.8)$$

where $d\Omega = \sin\theta d\theta d\phi$ and

$$F = \left| \int\int \frac{d\mathbf{r}_1}{a^3} \cdot \frac{d\mathbf{r}_2}{a^3} \phi_f^*\left(\frac{\mathbf{r}_1}{a}\right) \psi_f^*\left(\frac{\mathbf{r}_2}{a}\right) \cdot V'\left(\frac{\mathbf{r}_1}{a}, \frac{\mathbf{r}_2}{a}\right) \phi_i\left(\frac{\mathbf{r}_1}{a}\right) \psi_i\left(\frac{\mathbf{r}_2}{a}\right) \right|^2.$$

F is a definite integration over all space for $\mathbf{r}_1/a$ and $\mathbf{r}_2/a$, resulting in a definite number which represents a matrix element of the potential factor $(|\mathbf{r}_2/a - \mathbf{r}_1/a|)^{-1}$.

Remembering that $ak = 1/\sqrt{2}$ and taking $d\Omega = 4\pi$ we can write the transition probability as

$$W_A = C\frac{e^4 m}{\hbar^3},$$

where C is a numerical constant dependent on the various factors in W_A and F. Noting that $a_0 = \hbar^2/me^2$ and $v_0 = e^2/\hbar$, we have the simple relationship

$$W_A = Cv_0/a_0, \qquad (11.9)$$

where v_0 is the Bohr velocity, 2.2×10^8 cm/s, a_0 is the Bohr radius, 0.53 Å, and a_0/v_0 is a characteristic atomic time, 2.4×10^{-17} s. The integral F can be evaluated in the crude approximation $r_2 > r_1$ so that $1/|\mathbf{r}_2 - \mathbf{r}_1| \cong [1 + (r_1/r_2)\cos\theta_{1,2}]/r_2$, where $\theta_{1,2} = \theta_1 - \theta_2$. This approximation is based on the fact that the radial extension of the 1s wave function is small compared to the 2p function. The calculation

Table 11.2 Comparison of Auger Transition Rates and K level X-ray Emission Rates (Scofield) in eV/$\hbar$ (from Bambynek et al., 1972)

Atomic no.	Element	Auger	K X-ray
10	Ne	0.23	0.005
11	Na	0.29	0.007
12	Mg	0.36	0.010
13	Al	0.40	0.014
14	Si	0.44	0.02
15	P	0.48	0.03
16	S	0.51	0.04
17	Cl	0.54	0.05
18	Ar	0.58	0.07
20	Ca	0.65	0.12
22	Ti	0.69	0.19
24	Cr	0.72	0.28
26	Fe	0.75	0.40
28	Ni	0.78	0.55
32	Ge	0.83	1.0
36	Kr	0.89	1.69
40	Zr	0.94	2.69
46	Pd	0.99	4.94
52	Te	1.04	8.40
58	Ce	1.07	11.6
65	Tb	1.10	21.8
70	Yb	1.13	29.6

of C is tedious but straightforward; resulting in $C = 7 \times 10^{-3}$. The result for W_A [Eq. (11.9)] is independent of Z as suggested by Table 11.2. In a more complete calculation one must properly account for all the different equivalent pairs of electrons available for Auger decay. The calculations can be done more precisely via numerical techniques, which include more sophisticated wave functions and a better description of the interaction potential (Bambynek et al., 1972). The main feature is that the Auger transition probability is roughly independent of Z in contrast to the strong Z dependence of radiative transitions.

11.3 Yield of Auger Electrons and Fluorescence Yield

The lifetime of an excited state, τ, (a hole in a shell) is determined by the sum of all possible decay processes. Radiative transitions occur with probability W_X. Auger transitions have a probability W_A and Coster-Kronig (where the hole is filled by an electron of the same shell) W_K. There are no other deexcitation mechanisms, so that

$$1/\tau = W_X + W_A + W_K. \qquad (11.10)$$

For transitions to vacancies in the K shell (as well as for holes in the L_3 and M_5 shells), Coster-Kronig transitions do not occur and the probability for X-ray emission, ω_X, is given by

$$\omega_X = \frac{W_X}{W_A + W_X}; \qquad (11.11)$$

ω_X is commonly called the fluorescence yield. For transitions to K shell vacancies, the probability for radiative decay is proportional to Z^4 (Chapter 10), and the Auger probability is essentially independent of Z. Burhop[1] has suggested a semiempirical relation for ω_X of the form

$$\omega_X = \frac{W_X/W_A}{1 + W_X/W_A}, \qquad (11.12)$$

where

$$\frac{W_X}{W_A} = (-a + bZ - cZ^3)^4, \qquad (11.13)$$

[1] E. H. S. Burhop, *J. Phys. Radium* **16**, 625 (1955).

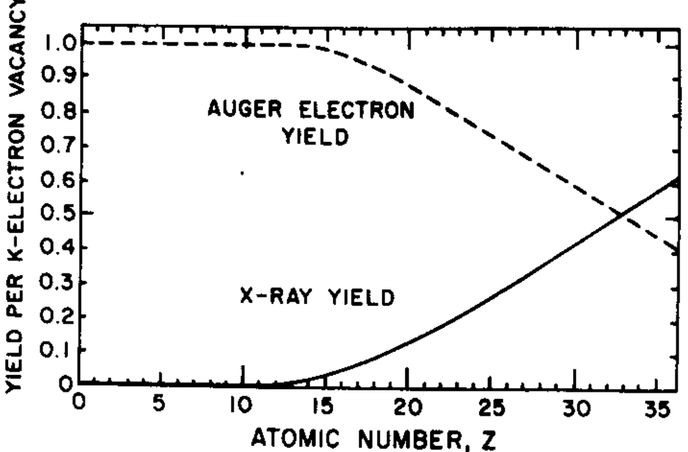

Figure 11.5 Auger electron and X-ray yields per K vacancy as a function of atomic number. The curves are from Eq. (11.12). [From Siegbahn et al., 1967.]

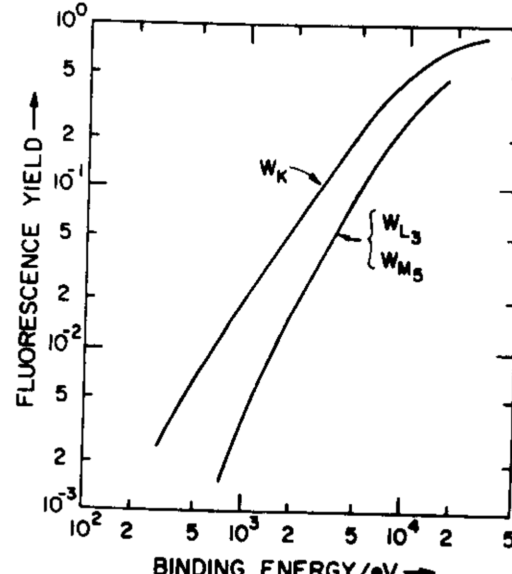

Figure 11.6 Fluorescence yield for K, L_3, and M_5 shells versus binding energy. [From J. Kirschner, in Ibach, 1977.]

with the numerical values $a = 6.4 \times 10^{-2}$, $b = 3.4 \times 10^{-2}$, and $c = 1.03 \times 10^{-6}$. This relationship yields the solid curve shown in Figure 11.5, the "Auger electron yield" is $1 - \omega_X$. This figure shows the dominance of Auger transitions for low Z elements; in these cases Auger emission is the important mechanism for relaxation of K vacancies. This curve does not imply that the Auger rate decreases at high Z, but emphasizes that the X-ray transition becomes the preferred method of deexcitation at high Z.

The fluorescence yield for K, L_3, and M_5 shells versus binding energy is shown in Figure 11.6. The point of the figure is that the fluorescence yield is approximately the same for comparable transition energies independent of the electronic shell, in those cases where Coster–Kronig transitions do not occur. For K shell transitions, the fluorescence yield is less than 0.1 for binding energies less than 2 keV, and the total Auger yield is larger than 90% for low Z elements ($Z < 15$). Similarly, for L_3 transitions (Coster–Kronig transitions not allowed), Auger transitions dominate for $Z < 50$ where L shell binding energies are less than 5 keV.

11.4 Atomic Level Width and Lifetimes

As pointed out in Chapter 10, the energy width ΔE or more conventionally Γ is related to the mean life τ of the state through the uncertainty principle, $\Gamma\tau = \hbar$. The decay probability per unit time is equal to the sum of the transition probabilities so that the total energy width of the state is given by

$$\Gamma = \Gamma_{\text{radiative}} + \Gamma_{\text{nonradiative}}. \tag{11.14}$$

There is a decay probability for each atomic process, but there is only a single lifetime for the hole. The natural linewidth for each process is given by the total lifetime. In the $Z < 30$ regime where Auger emission dominates, Table 11.2 shows that Auger rates vary from 0.23 to 0.80 eV/$\hbar$. The total width of the atomic transition then is 0.23–0.8 eV. For $Z > 30$, the K X-ray emission rates range up to 30 eV/$\hbar$ with a corresponding increase in atomic level width. The total lifetime $\tau = \hbar/\Gamma$, where $\hbar = 6.6 \times 10^{-16}$ s, will vary from about 10^{-17} to 10^{-15} s. Consequently, the measured X-ray spectrum will exhibit more line broadening at higher Z than at low Z, hence Al or Mg are used as X-ray sources for XPS.

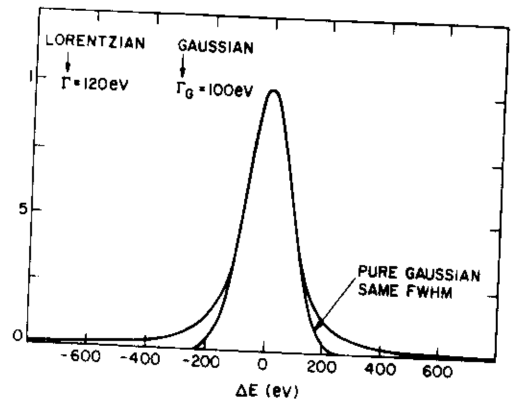

Figure 11.7 Comparison of a Lorentzian line shape [Eq. (11.15)] and a Gaussian line shape with the same full width and half maximum. The Lorentzian is characterized by extended tails.

An X-ray spectrum measured with high resolution would be in the form of a Lorentzian centered about an energy E_X (Figure 11.7):

$$Y(E) = \frac{A}{(E - E_X)^2 + \Gamma^2/4}. \tag{11.15}$$

11.5 Auger Electron Spectroscopy

As with the other electron spectroscopies, Auger analysis is carried out under high vacuum conditions. Figure 11.8 shows schematically an experimental apparatus. The cylindrical mirror analyzer (CMA) has an internal electron gun whose beam is focused to a point on the specimen sample at the source point of the CMA. Electrons ejected from the sample pass through an aperture and then are directed through the exit aperture on the CMA to the electron multiplier. The pass energy E is proportional to the potential applied to the outer cylinder, and the range ΔE of transmitted electrons is determined by the resolution $R = \Delta E/E$, where R is typically 0.2–0.5%.

A schematic overall spectrum of electrons emitted from a solid irradiated by a 2 keV electron beam is shown in Figure 11.9. The narrow peak on the right side is made up of elastically scattered electrons (no energy loss). Features at slightly lower energy correspond to electrons with characteristic energy losses due to electronic and plasma excitations. Auger electron transitions generally appear as small features superimposed on the large background of secondary electrons. The usual practice is to use derivative techniques and

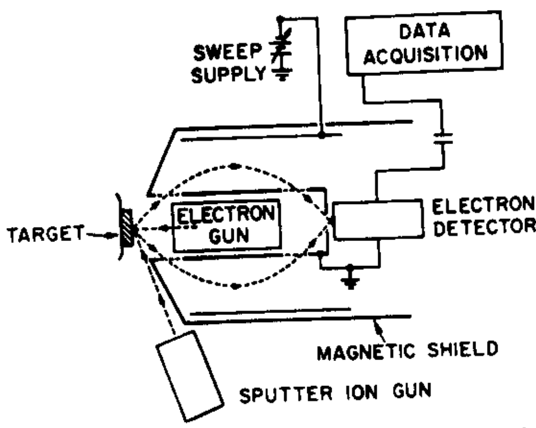

Figure 11.8 Experimental apparatus used in Auger spectroscopy. [After Palmberg in Czanderna et al., 1975.]

generate a dN(E)/dE function (insert on Figure 11.9). Differential analysis of a hypothetical spectrum is shown in Figure 11.10. The contribution from the slowly varying background is minimized by the derivative technique. The total backscattered background current with energy greater than 50 eV is typically 30% of the primary beam current. The noise level due to this current and the ratio of the analyzer ΔE to Auger line width generally establishes the signal-to-noise ratio and hence the detection limit for impurities in the sample. A typical value for the detection limit is 1000 ppm, ≅ 0.1 atomic %.

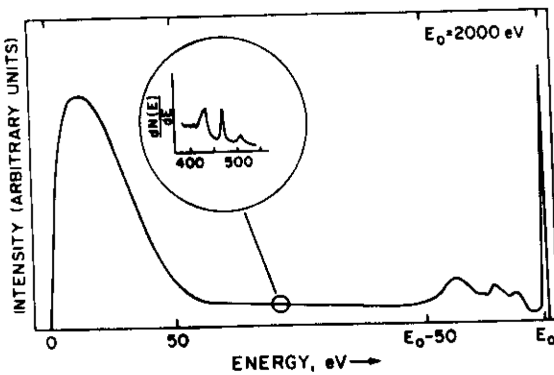

Figure 11.9 Spectrum of 2 keV electrons scattered from a solid. The inset shows the regime for Auger spectroscopy. The energy scale is nonlinear. [From Ibach, 1977.]

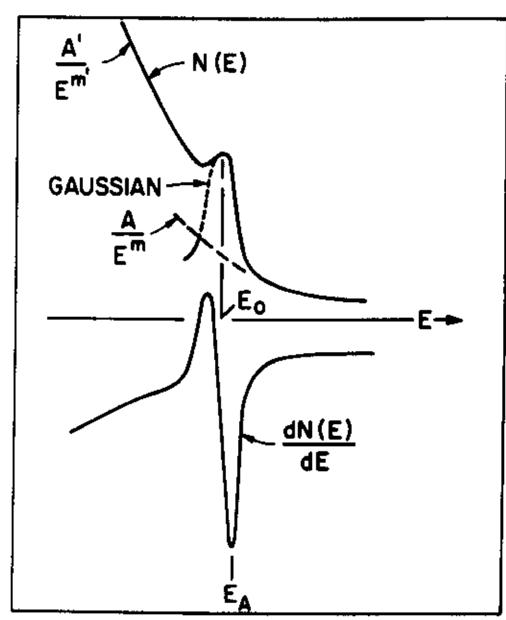

Figure 11.10 A hypothetical spectrum $N(E)$ containing a continuous background AE^{-m}, a Gaussian peak, and a low energy step of form $A'E^{-m'}$. The lower spectrum is the derivative spectrum. Note that the energy E_A of the most negative excursion of the derivative corresponds to the steepest slope of $N(E)$.

In practice, Auger spectroscopy is usually carried out in the derivative mode because of the small signal. The "differentiation" is conveniently done electronically by superimposing a small ac voltage on the outer cylinder voltage and synchronously detecting the in-phase signal from the electron multiplier with a lock-in amplifier. The y axis of the recorder is then proportional to $dN(E)/dE$ and the x axis to the kinetic energy E of the electrons. The derivative spectrum is extracted directly. In this scheme a perturbing voltage

$$\Delta V = k \sin \omega t \tag{11.16}$$

is superposed on the analyzer energy so that the collected electron current $I(V)$ is modulated. $I(V + \Delta V)$ can be written in a Taylor expansion:

$$I(V + k \sin \omega t) = I_0 + I'k \sin \omega t + k^2 \frac{\sin^2 \omega t}{2!} I'' + \cdots, \tag{11.17}$$

where the prime denotes differentiation with respect to V. Including higher order terms in the expansion

$$I = I_0 + \left[kI' + \frac{k^3}{8} I''' \right] \sin \omega t - \left[\frac{k^2}{4} I'' + \frac{k^4}{48} I'''' \right] \cos 2\omega t, \quad (11.18)$$

where I_0 contains all non-time-dependent terms. In this calculation we assumed $k \ll V$ so that terms of order k^3 and higher can be neglected in practice. Using a lock-in amplifier, for phase sensitive detection, we select the component of the signal associated with the frequency ω, which is simply the desired quantity I' or dN/dE for a cylindrical mirror Auger analyzer. To satisfy this criteria, we require that k be less than the Auger width of ~5 eV.

An example of the use of derivative techniques is shown in Figure 11.11 for 2 keV electrons incident on a Co sample. In the direct spectrum, n(E), the main features are the peak of elastically scattered electrons and a nearly flat background. The arrows in Figure 11.11a indicate the energies of oxygen and Co Auger transitions. The derivative spectrum (Figure 11.11b) reveals the LMM Co and KLL carbon and oxygen signals.

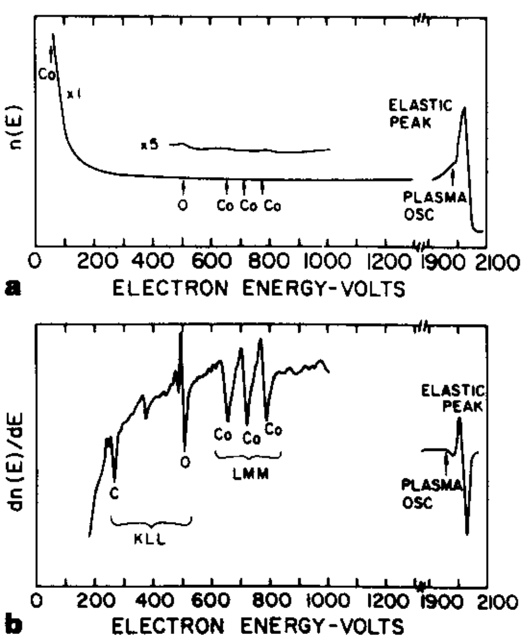

Figure 11.11 Comparison of (a) the spectrum N(E) and (b) the derivative dN(E) for 2 keV electrons incident on a Co sample. [From Tousset, in Thomas and Cachard, 1978.]

For a free atom, the Auger yield Y_A is determined by the product of the electron impact ionization cross section (Chapter 6) and the probability for the emission of an Auger electron $(1 - \omega_X)$:

$$Y_A \propto \sigma_e \cdot (1 - \omega_X). \quad (11.19)$$

In a solid, the situation is more complicated even when considering the yield from a layer of the thickness of the electron escape depth λ. For example, primary electrons that penetrate the surface layer and then are backscattered can contribute to the Auger yield when the energy E_p of the primary electron is much greater than the binding energy. The yield is also strongly affected by the angles of incidence (diffraction effects influence the number of elastically scattered primaries) and of emission (geometric projection of the escape depth). Consequently, surface roughness plays a role; the escape probability of electrons from a rough surface is less than that from a smooth surface. In analyzing solids, then, one must consider the modification of both the incident beam and the Auger electrons on passing through the solid.

Auger electron spectroscopy is a surface sensitive technique. Figure 11.12 shows the oxygen signal corresponding to the absorption of 0.5 monolayers of oxygen atoms. In general, small amounts of the typical contaminants, C, N, and O, are easily detected. Hydrogen cannot be detected in Auger measurements since 3 electrons are needed in an Auger transition.

The Auger signal from a substrate is sensitive to the presence of surface layers. In Chapter 6, we noted that the substrate signal de-

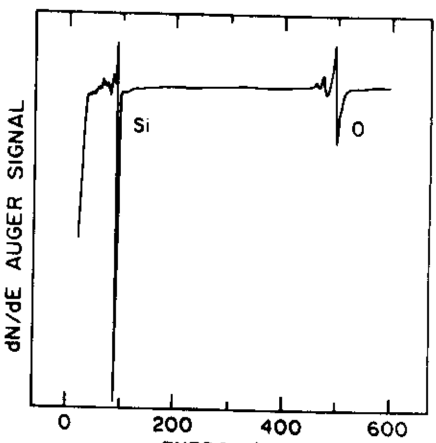

Figure 11.12 Auger spectra from single crystal Si (111) after adsorption of ~0.5 monolayers of oxygen atoms.

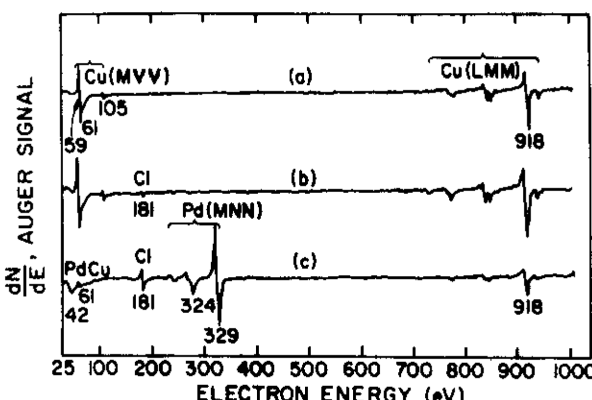

Figure 11.13 Auger traces of (a) freshly deposited Cu substrate, (b) Cu substrate just prior to Pd deposition, and (c) Pd/Cu bilayer, 13.5 Å of Pd.

creased as $e^{-x/\lambda}$, where $\lambda = 5$ Å for Si electrons penetrating Ge. Figure 11.13 shows Auger spectra from a Cu substrate before and after the deposition of 13.5 Å of Pd. It is clear from the figure that the Cu signal is strongly attenuated by the Pd coverage. In particular, the low energy Cu(MVV) line is completely attenuated due to the small escape length for 60 eV electrons; the high energy line at 918 eV is only partly attenuated.

11.6 Quantitative Analysis

The determination of an absolute concentration of an element x in a matrix from the yield Y_A of Auger electrons is complicated by the influence of the matrix on the backscattered electrons and escape depth. For simplicity let us consider $Y_A(t)$ the yield of KLL Auger electrons produced from a thin layer of width Δt at a depth t in the sample.

$$Y_A(t) = N_x \Delta t \cdot \sigma_e(t)[1 - \omega_X]e^{-(t\cos\theta/\lambda)} \cdot I(t) \cdot T \cdot d\Omega/4\pi, \quad (11.20)$$

where

N_x = the number of x atoms/unit vol;

$\sigma_e(t)$ = the ionization cross section at depth t;

ω_X = the fluorescence yield;

λ = the escape depth;

θ = the analyzer angle;

T = the transmission of the analyzer;

$d\Omega$ = the solid angle of the analyzer;

$I(t)$ = the electron excitation flux at depth t.

It is convenient to separate the excitation flux density into two components,

$$I(t) = I_P + I_B(t) = I_P(t)[1 + R_B(t)],$$

where I_P is the flux of primary electrons at depth t and I_B is the flux due to backscattered primary electrons and R_B is the backscattering factor (Section 10.7).

When external standards are used with a known concentration N_x^S of element x in the standard, the concentration N_x^T in the test sample can be found from the ratio of Auger yields:

$$\frac{N_x^S}{N_x^T} = \frac{Y_x^S}{Y_x^T}\left(\frac{\lambda^T}{\lambda^S}\right)\left[\frac{(1 + R_B^T)}{(1 + R_B^S)}\right].$$

In this approach the ionization cross section and the fluorescence yield are not required because the Auger yields from the same atom are measured. In addition, if the composition of the standard is close to that of the test sample, the element composition can be determined directly from the ratio of Auger yields if the measurements are made under identical experimental conditions. When the composition of the standard differs substantially from that of the test specimen, the influence of the matrix on electron backscattering and escape depth must also be considered.

Elemental sensitivities are acquired using pure element standards and are applied to unknown determinations in multielemental matrices. One must correct for the highly matrix-dependent parameters, which include the inelastic mean free path λ.

Even with corrections for escape depth and backscattering, the measured surface composition may not be related to the bulk composition of the sample because of the ion bombardment used in sputtering for sample cleaning and depth profiling (see Chapter 4).

11.7 Auger Depth Profiles

A major use of Auger electron spectroscopy is determining the composition as a function of depth in thin films and layered structures. The conventional apparatus is illustrated in Figure 11.8, which consists of an electron gun and CMA assembly ...

gun. The Auger signal is generated in the near surface region of the sample (~ 30 Å) and ion sputtering provides the layer sectioning technique required for depth analysis. In routine laboratory use, the depth profiles are shown as Auger signal height versus sputter time. Further calibrations are required to convert sputter time to depth and signal height to atomic concentration. The combination of Rutherford backscattering spectrometry (RBS) and Auger electron spectroscopy (AES) is quite useful in such depth profile analyses because RBS gives quantitative information on depths and heavy mass constituents without the complications introduced by the intermixing due to sputtering. As discussed in Chapter 4, ion sputtering causes a change in the composition of the surface layers due to surface segregation and preferential sputtering. As compared to RBS, Auger depth profiling provides better depth resolution and is sensitive to both heavy and light elements.

In Figure 11.14 we illustrate the data obtained from RBS and AES measurements on a sample prepared by depositing 1000 Å of Ni on ⟨100⟩ InP (Figure 11.14a) and annealing at 250°C for 30 min (Figure 11.14b). In the RBS spectrum for the as-deposited case, the Ni signal is superimposed on the signal from the InP substrate. In the AES spectrum, both the In and P signals have comparable heights and can be clearly resolved. The long tail on the Ni signal which extends well beyond the interface region is clearly an artifact of the sputtering process because the Ni/InP interface is sharp, as can be inferred from the rear edge of Ni signal in the RBS spectrum. After annealing, the layer is partially reacted with an outer layer of Ni on a layer of $In_xP_yN_z$. The Ni layer and the reacted InPNi layer can be clearly seen in the AES spectrum, which has a P/In yield ratio of ≃ 2/1. In the RBS spectrum, the heights of the Ni and In signals are nearly equal, which indicates that the ratio of Ni to In is about 3 [$\sigma_{In}/\sigma_{Ni} \simeq 3.08$]. Analysis of the RBS spectra yields a P/In ratio of 0.5, a value quite different from the P-rich composition deduced from the AES data. The origin of the discrepancy possibly is due to preferential sputtering and segregation. The region of pure Ni in the reacted film is better resolved with AES due to its superior depth resolution. Further AES allowed a determination of the carbon and oxygen at the interface region (not shown), which is not possible with RBS.

One of the advantages of Auger electron spectroscopy is its sensitivity to low mass impurities, such as carbon or oxygen, which are common contaminants at surfaces and interfaces. The presence of these interfacial contaminants plays a disruptive role in thin film reactions by retarding interdiffusion. The degradation of the planar-

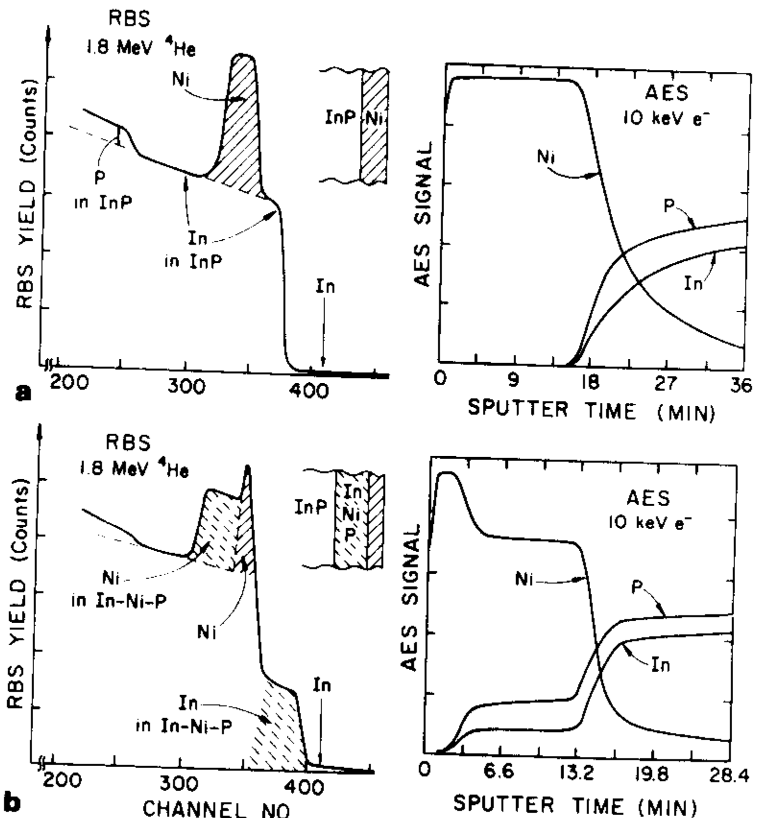

Figure 11.14 Comparison of RBS (left) and AES depth profiles of a 1000 Å Ni deposited on InP: (a) as deposited; (b) annealed at 250°C for 30 min. [From A. Appelbaum, private communication.]

ity of thin film structures following thermal processing is often directly correlated with these contaminants. The presence of a native oxide of about 15 Å thickness is readily apparent in the AES depth profile shown in Figure 11.15. The removal of this native oxygen layer is crucial for the formation of thin, uniform oxide layers on top of the Ta-silicide layers during thermal oxidation. The presence of the native oxide layer retards the release of Si from the poly-Si layer and leads to the oxidation of the whole Ta-silicide layer rather than the formation of a SiO_2 layer on the surface. Auger electron spectroscopy in conjunction with sputter depth profiling has the prerequisite sensitivity to detect contaminant layers that impede thin film reactions.

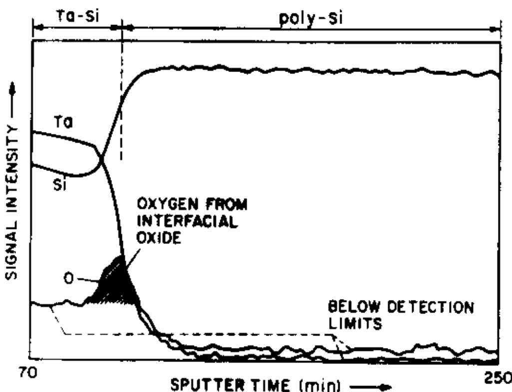

Figure 11.15 Sputter depth profiling with AES of the interface region of a Ta-Si film deposited on polycrystalline Si. The shaded area represents the oxygen signal from the native oxide at the interface. [From D. Pawlik, H. Oppolzer, and T. Hillmer, *J. Vac. Sci. Technol.* B **3**, 492 (1985).]

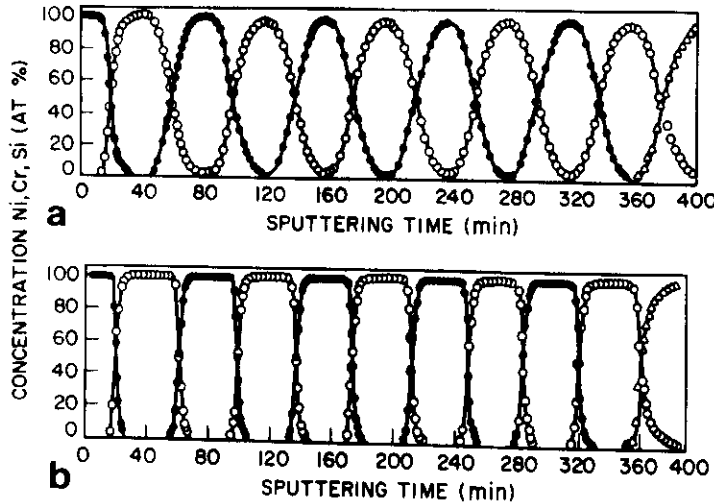

Figure 11.16 Auger electron spectroscopy sputter depth profiles of multilayer Cr/Ni thin film structures deposited on a Si substrate. The top Ni layer is about 250 Å thick and the other films are about 500 Å thick. Sputtering was carried out with a rastered beam of 5 keV Ar ions with a stationary sample in the upper portion (a), and a rotating sample in the lower portion (b). The symbols represent: ● nickel; ○ chromium; △ silicon. [From A. Zalar, *Thin Solid Films* **124**, 223 (1985).]

Multilayer films are used in integrated circuits and optical structures as well as in many other aspects of solid-state science. Auger electron spectroscopy with sputter depth profiling has a natural application to the analysis of these structures.

Figure 11.16 shows sputter depth profiles of multilayer Cr/Ni thin film structures deposited in a Si substrate. This impressive figure demonstrates the ability of Auger spectroscopy, combined with sputtering, to profile a multilayer film of nearby elements in the periodic chart in a semiquantitative manner. The rounding in the traces in the upper portion of the figure reflects the irregularity in the surface topology that developed during sputtering with a rastered beam of 5 keV Ar ions (see Chapter 4 and Carter et al., 1983). In this example, the surface roughness could be minimized by rotating the sample (lower portion of Figure 11.16) during sputtering.

Modern analytical laboratories are now equipped with a variety of systems for depth profiling of samples. When confronted with a layered or thin film sample containing unknown impurities or contaminants, the analyst will use all techniques at hand. Sputter depth profiling with Auger analysis often represents the starting point for initial analyses.

Problems

11.1. You irradiate an AlP sample with 5 keV electrons and measure the KLL Auger electrons. Calculate the ratio of Al to P ionization cross sections; fluorescence yields ω_X; escape depths λ; and Auger yields.

11.2. Compare the Auger yields in Problem 11.1 with the electron microprobe K X-ray yields ignoring X-ray absorption or electron backscattering corrections.

11.3. A Mg K_α X-ray creates a vacancy in the Cu $L_1(2s)$ subshell. Estimate the energies of photoelectrons, LM_1M_1 Auger electrons, $L_1L_2M_1$ Auger electrons (Coster-Kronig transitions), and L X-rays. Would this L shell vacancy preferentially be filled by radiative or nonradiative transitions and make an estimate of the upper value of the fluorescence yield? Which Cu L level would not deexcite by Coster-Kronig transitions?

11.4. A beam of 10 keV electrons irradiates a 1000 Å thick film of Ni on a Si substrate. Calculate the ratio of K X-ray and KLL Auger yields.

11.5. You are given a 200 Å thick layer of $Ga_xAl_{1-x}As$ on an InP substrate about 1 mm thick and are asked to determine the Ga to Al ratio. You can carry out XPS, AES or EMA analysis using 20 keV electrons and an Al K_α X-ray source. In order to compare the different techniques, you carry out the following calculations or comparisons.
(a) What is the cross section ratio σ_{Ga}/σ_{Al} for the K shell electron impact ionization and L shell photoeffect?
(b) What is the fluorescence yield ratio $\omega_X(Ga)/\omega_X(Al)$ for the K shell hole?
(c) You measure the intensity of the K_α X-ray emission from Ga and Al with a detector system with 200 eV resolution. Would you expect interference from K, L_α or M X-rays from As atoms or from the InP substrate? Would you expect electron backscattering from the InP substrate to influence the total or the ratio of X-ray yields from Ga and Al?
(d) In XPS measurements (neglecting work functions) what are the Ga and Al photoelectron energies and associated escape depths (λ)? What is the intensity ratio assuming the same detector efficiency for both electron energies?
(e) In measurements of KL_1L_1 Ga and Al Auger electrons, what are the energies and associated escape depths? What is the ratio of Ga to Al transition rates?
(f) Compare the three techniques in terms of analysis depth, corrections or interferences, and yield ratios for values of x near 0.9.

11.6. Compare transitions for K shell holes in Z = 20 and Z = 36 elements.
(a) What are the W_X/W_A ratios [Eq. (11.13)]? Compare these values with the curve in Figure 11.5.
(b) What are the atomic level widths and lifetimes? Compare the lifetime values for the two elements with the time for an electron to make a circular orbit in the Bohr model of the atom.

11.7. In an XPS analysis system with an Al K_α X-ray source, Auger electrons as well as photoelectrons are detected (see, for example, Figure 9.7). For a vanadium target, what would be the energies and escape depths of the 2s photoelectrons and L_1MM Auger electrons? In comparison with 1.5 keV electrons, what is the ratio of electron to photon cross sections, σ_e/σ_{ph}, to form a 2s hole? The L shell fluorescence yield is small (Appendix 8 or Figure 11.6), so estimate the ratio of photoelectron to Auger electrons assuming Coster–Kronig transitions can be neglected. Is this a good assumption?

References

1. W. Bambynek et al., X-ray Fluorescence Yields, Auger and Coster–Kronig Transitions, *Rev. Mod. Phys.* **44**, 716 (1972).
2. T. A. Carlson, *Photoelectron and Auger Spectroscopy* (Plenum Press, New York, 1975).
3. G. Carter, B. Navinšek, and J. L. Whitton, "Heavy Ion Surface Topography Development" in *Sputtering by Particle Bombardment II*, R. Behrisch, Ed. (Springer-Verlag, Berlin, 1983).
4. C. C. Chang, "Analytical Auger Electron Spectroscopy" in *Characterization of Solid Surfaces*, P. F. Kane and G. R. Larrabee, Eds. (Plenum Press, New York, 1974), Chap. 20.
5. A. W. Czanderna, Ed., *Methods of Surface Analysis* (Elsevier, Amsterdam, 1975).
6. L. E. Davis, N. C. MacDonald, P. W. Palmberg, G. E. Riach, and R. E. Weber, *Handbook of Auger Electron Spectroscopy* (Physical Electronics Industries, Inc., Eden Prairie, MN, 1976).
7. G. Ertl and J. Kuppers, *Low Energy Electrons and Surface Chemistry* (Verlag Chemie International, Weinheim, 1974).
8. G. Herzberg, *Atomic Spectra and Atomic Structure* (Dover, New York, 1944).
9. H. Ibach, Ed., *Electron Spectroscopy for Surface Analysis*, Topics in Current Physics, Vol. 4 (Springer-Verlag, New York, 1977).
10. A. Joshi, L. E. Davis, and P. W. Palmberg, "Auger Electron Spectroscopy" in *Methods of Surface Analysis*, A. W. Czanderna, Ed. (Elsevier Science Publishing Co., New York, 1975), Chap. 5.
11. G. E. McGuire, *Auger Electron Spectroscopy Reference Manual* (Plenum Press, New York, 1979).
12. K. D. Sevier, *Low Energy Electron Spectroscopy* (Wiley-Interscience, New York, 1972).
13. K. Siegbahn, C. N. Nordling, A. Fahlman, R. Nordberg, K. Hamrin, J. Hedman, G. Johansson, T. Bergmark, S. E. Karlsson, I. Lindgren, and B. Lindberg, *ESCA, Atomic, Molecular and Solid State Structure Studied by Means of Electron Spectroscopy* (Almqvist and Wiksells, Uppsala, Sweden, 1967).
14. J. P. Thomas and A. Cachard, Eds., *Material Characterization Using Ion Beams* (Plenum Press, New York, 1978).

SURFACE ANALYSIS TECHNIQUES

Method	Particle Measured	Process	Information	Monolayer Sensitivity	Effective Probing Depth	Depth Profiling
Auger Emission Spectroscopy (A.E.S.)	Auger Electrons		—Elements Li-U	10^{-1}	20 Å	In Combination with Sputtering
Scanning Electron Microscopy-Energy Dispersive X-Ray (SEM-EDX)	X-Rays		—Elements Na-U	None	10000 Å	None
Transmission Electron Microscopy (TEM)	Diffracted Electrons		—Compound Identification	None	500 Å	None
X-Ray Photo Electron Spectroscopy (XPS or ESCA)	Photo Electrons		—Elements Li-U, —Chemical Bonding	10^{-1}	30 Å	None
Secondary Ion Mass Spectrometry (SIMS)	Sputtered Ions		—Elements H-U	10^{-5}	10 Å	Via Sputtering
Rutherford Backscattering Spectrometry (RBS)	Scattered Ions (H^+, He^+)		—Eleme[illegible] Be-U	10 - 10^{-4}	100 Å	Via Energy Loss
Particle Induced X-Ray Emission (PIXE)	X-Rays		—Elements Na-U	None	1000 Å - 10000 Å	None
Nuclear Reaction Analysis (NRA)	Light Ion Reaction Product		—Light Elements (H, Be, B, C O, F...)	10^{-1}	100 Å - 10000 Å	Via Energy Loss